Diploma Thesis

Realization of an active magnetic bearing for a flywheel energy storage

Manes Recheis

Institute of Electrical Measurement and Measurement Signal Processing
Univerity of Technology Graz
Head of the Institute: Univ.-Prof. Dipl.-Ing. Dr. techn. Georg Brasseur

Assessor: Dipl.-Ing. Dr. techn. Hannes Wegleiter

Graz, 28th of December, 2010

Abstract

Hybrid drive concepts compared to conventional concepts provide a significant higher level of efficiency. This is possible due to selective load level adjustment of the internal combustion engine and downsizing. Additionally, the electrified power train provides partially brake energy recuperation. Modern hybrid drive concepts use lithium-ion batteries or ultra-cap modules for energy storage. Both technologies are not adequate for this duty.

Batteries come with marginal power density and cycle consistency and lead to big and heavy solutions for the required amount of energy. On the one hand ultra-cap modules provide a much higher power density, but on the other hand the energy density is not satisfying. Therefore a lot of space is needed for the required amount of energy which is hard to find in vehicles. Additionally, the operation area of both technologies is limited to critical temperatures and therefore a sophisticated cooling system is inevitable.

A flywheel combines both, a high power density and a high energy density. Therefore it represents a useful supplement to present energy storage systems. In order to provide a high energy density, high rotational speeds are required. To reduce stand-by friction losses to air at high rotational speeds, the flywheel is being operated in vacuum. Since lubrication in vacuum is difficult and high rotational speeds damage the bearings, a magnetic bearing enables rotation nearly without any losses. The maximum rotational speed is theoretically only limited by the mechanical strength of the rotor that has to bear the centrifugal load.

A magnetic bearing for a flywheel energy storage in a vehicle should establish a long live-span with nearly endless cycles combined with accurate operating costs.

Kurzfassung

Hybride Antriebskonzepte bieten, im Vergleich zu konventionellen Antriebskonzepten, den Vorteil eines signifikant erhöhten Wirkungsgrades. Dies ist durch gezieltes "downsizing" sowie einer Lastpunktverschiebung der Verbrennungskraftmaschine möglich. Zusätzlich erlaubt die Elektrifizierung des Antriebsstranges ein elektrisches Bremsen und somit eine Teilrückgewinnung der Bremsenergie. Aktuelle Hybridlösungen verwenden größtenteils Lithium-Ionen Batterien oder Ultra-Cap Module als elektrischen Energiespeicher. Beide Technologien sind jedoch nur bedingt für diese Aufgabe geeignet.

Batterien verfügen über eine geringe Leistungsdichte und Zyklenfestigkeit. Die benötigten Energiemengen führen zu - für mobile Anwendungen verhältnismäßig - schweren Lösungen mit zu großem Volumen. Ultra-Caps besitzen zwar eine wesentlich höhere Leistungsdichte, jedoch eine vergleichsweise geringe Energiedichte. Damit ergeben sich wiederum große Volumen und Massen für die geforderten Energiemengen welche im Fahrzeug nur schwer Platz finden. Durch den eingeschränkten Arbeitstemperaturbereich benötigen beide Systeme zusätzlich aufwendige Kühlsysteme.

Ein mechanischer Schwungradspeicher kombiniert eine hohe Leistungsdichte mit einer hohen Energiedichte und stellt damit eine sinnvolle Ergänzung zu bestehenden elektrochemischen Energiespeichern dar. Um bei geringem Gewicht verhältnismäßig große Energiemengen zu speichern, benötigt man sehr hohe Drehzahlen. Um die Leerlaufverluste dabei möglichst gering zu halten werden, wird das Schwungrad in Vakuum betrieben. Eine mechanische Lagerung ist aufgrund der begrenzten Schmiermöglichkeiten im Vakuum schwer realisierbar. Magnetschwebelager hingegen ermöglichen einen Betrieb ohne Lagerreibungen. Die maximal realisierbare Drehzahl des Schwungrades ist somit theoretisch nur durch die Festigkeit des Rotors gegenüber den auftretenden Fliehkräften begrenzt.

Der Einsatz eines Magnetschwebelagers in einem KFZ[1] soll die mechanischen Belastungen durch die im Betrieb auftretenden Kräfte bei ausreichender Lebensdauer zu vernünftigen Kosten ermöglichen.

[1] Kraftfahrzeug

Statutory Declaration

I declare that I have authored this thesis independently, that I have not used other than the declared sources / resources, and that I have explicitly marked all material which has been quoted either literally or by content from the used sources.

Graz	December 28th, 2010	
Place	Date	Signature

Eidesstattliche Erklärung

Ich erkläre an Eides statt, dass ich die vorliegende Arbeit selbstständig verfasst, andere als die angegebenen Quellen/Hilfsmittel nicht benutzt und die den benutzten Quellen wörtlich und inhaltlich entnommene Stellen als solche kenntlich gemacht habe.

Graz	28. Dezember 2010	
Ort	Datum	Unterschrift

Contents

List of Figures

[2]Quantile-Quantile

List of Tables

Chapter 1

Introduction

In the year of 1900 the first hybrid car built by Lohner-Porsche was presented successfully at the World Exhibition in Paris. This car used an internal combustion engine driving at constant speed to power an electrical generator which charged several accumulators. These fed electric current to the electric hub motors in the front wheels.

Figure 1.1: "Lohner-Porsche Mixte" hybrid car, developed in 1899 [2]

The automobile world was astonished by this novelty and other manufacturers followed producing hybrid cars. The reason for their early success is that other than combustion cars, the hybrid cars did not need to be started by hand with a crank, which was quite exhausting at that time. Since cars were only affordable for privileged people this comfort was crucial. When the first electric starters for combustion engine vehicles came up

around 1920, the success of hybrid drive technology came to a temporary stop.

1.1 Kinetic Energy Storage

Hybrid drive concepts compared to conventional concepts provide a significant higher level of efficiency. This is possible due to selective load level adjustment of the internal combustion engine and downsizing. Additionally, the electrified power train provides partially brake energy recuperation. Modern hybrid drive concepts use lithium-ion batteries or ultra-cap modules for energy storage. Both technologies are not adequate for this duty.

Batteries come with marginal power density and cycle consistency and lead to big and heavy solutions for the required amount of energy. On the one hand ultra-cap modules provide a much higher power density, but on the other hand the energy density is not satisfying. Therefore a lot of space is needed for the required amount of energy which is hard to find in vehicles. Additionally, the operation area of both technologies is limited to critical temperatures and therefore a sophisticated cooling system is inevitable.

A flywheel combines both, a high power density and a high energy density. Therefore it represents a useful supplement to present energy storage systems. In order to provide a high energy density, high rotational speeds are required. To reduce stand-by friction losses to air at high rotational speeds, the flywheel is being operated in vacuum. Since lubrication in vacuum is difficult and high rotational speeds damage the bearings, a magnetic bearing enables rotation nearly without any losses. The maximum rotational speed is theoretically only limited by the mechanical strength of the rotor that has to bear the centrifugal load. A magnetic bearing for a flywheel energy storage in a vehicle should establish a long live-span with nearly endless cycles combined with accurate operating costs.

1.2 Electric Energy Storage Methods

Electric energy, which features the highest exergy of all sources of energy, has to be produced demand oriented. For this reason storing electric energy has been a challenge since several hundreds of years. It all began in the year 1800 with Alessandro Volta, who constructed the first documented electro-chemical energy storage.
The following list summarizes possible methods to store electrical energy. Methods that are not appropriate for mobile applications were omitted for lucidity.

- Electrical energy storage:

  - ⋆ EDLC[1]: Based on their low energy density, supercaps require much space and are expensive which leads to the high capital costs. They can be cycled several hundred thousands of times and can be loaded or unloaded in seconds. Self-discharge is beneath 1% per hour and the storage efficiency is about 90%. Electrolyte capacitors lead to outstanding capital costs combined with very low energy density compared to other methods in this list.
  - ⋆ SMES[2]: The energy density compared to EDLC is ten times higher and the stored energy is available faster. The investment costs are also lower than those of EDLC storages. A big disadvantage is that a part of the energy is needed to cool the coil, which decreases the level of efficiency.[12]

- Mechanical energy storage: Mechanical energy is either stored as kinetic energy or potential energy.
  - ⋆ Flywheel: There are two kinds of flywheels. Mechanical flywheels and electromechanic flywheels. The comparison in table 1.1 features the electromechanic flywheel, which is discussed further in section 1.3. High speed flywheels, constructed with fiber-reinforced composite materials, can compete with SMES in power density and feature a high energy density. Additionally, they enable mobile applications due to light weight construction.
  - ⋆ CAES[3]: Adiabatic compressed air energy storage solutions to store wind power reach up to 70% level of efficiency. This includes regaining the compression heat losses. For mobile applications regaining compression heat is too difficult. The typical level of efficiency therefore is in the range of 50%.

- Chemical energy: [17]
  - ⋆ Redox flow accumulator: This method uses an external storage of two different liquid electrolytes. The energy density is comparable to lead acid batteries but the cycle consistency is ten times higher. An interesting fact is that this kind of battery can be refueled with new electrolyte. A typical application could be refueling for electric cars. The overall level of efficiency is approximately 70 %.
  - ⋆ Lead-acid accumulator: This most widely used technology has a low energy density and a low cycle consistency. Beside the application as starter battery lead acid batteries are often used for grid stabilization, especially at isolated operation, and for UPS[4].

[1] Electric double layer capacitor, a.k.a. supercap or ultracap
[2] Superconducting magnetic energy storage
[3] Compressed air energy storage
[4] Uninteruptible power supply

  - ⋆ Lithium ion accumulator: Since many different cathode and anode material configurations are existing, lithium ion cells are difficult to compare. There are some interesting configurations like lithium-titanate, lithium-air and lithium-iron-phosphate cells that have the potential to compete with the energy densities and power densities of typical steel flywheels.
  - ⋆ High temperature NaNiCl- and NaS-batteries: Compared to other types these batteries benefit from a higher cycle consistency, but they need to be operated at 290 to 390 °C. The Tokyo Electric Power Company runs a 6 MW load leveling plant with 48 MWh balancing energy [18].

- Thermal energy: Since thermal energy is the lowest of all energy levels, thermal energy storage is mostly relevant for district heating and warm water supply.

Tabular 1.1 compares the discussed energy storage types based on their specific power (SP), specific energy (SE), cycle-time (t_{cycle}), durability, total level of efficiency η, self-discharge and capital costs (CC).

type	method	SP	SE	t_{cycle}	durability	η	self-discharge	CC
		$\frac{W}{kg}$	$\frac{Wh}{kg}$		cycles	%	$\frac{\%}{h}$	$\frac{€}{kWh}$
electric	capacitor	<10k	>0.1	<0.1s	100M	≈95	0.01	>10k
electric	EDLC	<10k	<10	>1s	500k	≈90	0.2	>1k
electric	SMES	<10k	<100	<0.1s	1M	≈90	0	<2k
mechanic	flywheel	<2.0k	<50	3s-15m	1M	≈90	1	<2k
chemic	Pb-acid acc.	<4.1k	<70	1h	<42k	80-90	0.04	<250
chemic	Li-ion acc.	<1.8k	<190	1h	>1k	70-90	0.001	<1k

Table 1.1: Energy storage types for mobile applications in comparison

In figure 1.2 energy storage technologies are compared in the gravimetric ragone chart. An important fact is that the chart in figure 1.2 does not take the total level of efficiency into account.

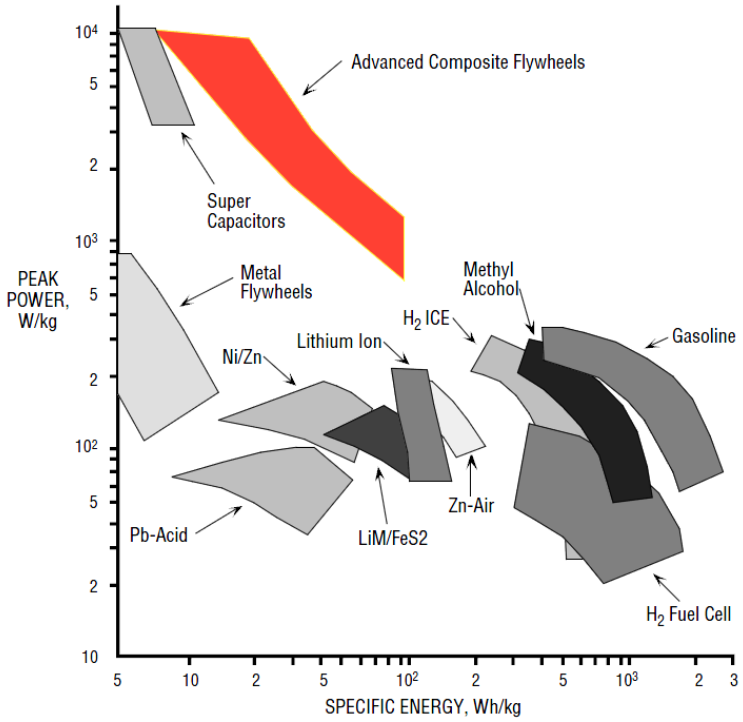

Figure 1.2: Gravimetric ragone chart of energy storage technologies [16]

1.3 Existing Flywheel Energy Storages

Flywheel energy storages have been built around the world to store and deliver high power for short periods of time. Static applications are stabilizing power transmission grids, peak power supply and UPS. The unique mobile application is storing recuperational brake energy. AMB[5] technology is commonly used in the latest flywheel storages. An exception is the motorsport industry that uses high speed flywheels with hybrid ceramic bearings due to weight reduction [4]. For high speed flywheels an evacuated housing is indispensable to reduce air friction. This means that the rotor's power dissipation has to be minimal since radiation is the only way to emit heat.

There are three different rotor stator configurations for electromechanic flywheel energy storage systems:

- Internal rotor: This type benefits from a simple construction where the stator represents the whole evacuated housing and also contains the AMB components. Another advantage is that the rotor-stator air gap is a minimum at operating temperature and maximum rotational speeds. Since the rotor's geometry and construction is predefined and thus based on the electric machine, design parameters are limited.

[5] Active magnetic bearing

- External rotor: This configuration features a larger rotor surface in contrast to the internal rotor and therefore benefits from better heat radiation. Additional high-strength composite fiber material, surrounding and therefore reinforcing the rotor, enables high speed operation. A disadvantage is that the construction is more complex because the evacuated housing has to be built around the external rotor.
- Internal rotor with external flywheel: This most widely used type combines the advantages of the previous mentioned types. Additionally, the desired inertia can be designed independently.

The best electric machines for flywheels are PMSM[6]s, also called brushless-DCs, and switched reluctance machines, also called SRM[7]s. On the one hand the permanent magnet synchronous machine features the highest gravimetric and volumetric power density. On the other hand its permanent magnets lose their strength when overheated. The switched reluctance machine provides constant torque at any speed and the rotor is insensitive to overheating, although it cannot compete in power density.

The data in tabular 1.2 cannot always be trusted. Most companies do not provide exact data. For instance the "weight" is not clearly clarified as overall system weight, and therefore sometimes just the rotor weight is mentioned.

[6]Permanent magnet synchronous motor
[7]Switched reluctance machine

name	company	n	P	E	M	SP	SE	V	PD	ED	t	appl.	bearing	config.	η
		rpm	kW	kWh	kg	$\frac{W}{kg}$	$\frac{Wh}{kg}$	m^3	$\frac{W}{l}$	$\frac{Wh}{l}$	s				%
T1 [3]	Rosseta	25.500	150	2	540	278	3,7	0,65	230	3	48	stat.	cer.+PM[a]	ext.FW[b]	
T2 [3]	Rosseta	25.000	500	4	650	769	4,2	1,12	447	3,6	29	stat.	cer.+PM	ext.FW	89
T3 [3]	Rosseta	6.000	3	0,0058	60	50	0,1	0,162	19	0,036	7	stat.	cer.+PM	ext.FW	84
T4 [3]	Rosseta	25.000	100	5	450	222	11	0,745	134	6,7	180	stat/mob.	cer.+PM	ext.FW	88
MDS K5	Alstom, L3-MM[c]	12.000	200	2	1120	179	1,8	3,34	60	0,6	36	mob.	-	-	<90
MDS K6	Alstom, L3-MM	21.000	450	6	1300	346	4,6	3,34	135	1,79	48	mob.	-	-	<90
MDS 12	ATZ, L3-MM	10.000	250	10	1200	208	8,3	0,95	263	10,5	144	stat.	HTSMB[d]	ext.FW	92
EMAFER	CCM	17.000	300	3,11	783	383	4	xxx	XX	XX	37	mob.	konv.	-	-
Ulev Tap 1	CCM	15.000	300	4	850	353	4,7	0,573	524	7	48	mob.	con.	-	-
Ulev Tap 2	CCM	22.000	300	4	375	800	10,7	0,215	1395	18,6	48	mob.	con.	-	96
Power Bridge	Piller[e]	3.300	1200	4	7000	171	0,6	3,5	340	1,1	12	stat.	con.+PM	ext.FW	93
Experiment	Dynastore	10.000	2000	11	1200	1666	9,2	1,06	1886	10,3	20	stat.	SMB	ext.	94
Nedo	Japan	15.860	15	10	425	35	24	1,97	8	5	2400	stat.	AMB	int.	-
KERS	Compact Dynamics	100.000	90	0,75	40	2250	19	0,023	3858	32	30	mob.	int.	conv.	-
GTX UPS	Pentadyne[f]	55.000	200	0,68	590	339	1,2	0,094	2125	7,2	12,3	stat.	AMB	ext.FW	-
Trinity	Trinity[g]	-	125	0,7	175	714	4	0,04	2998	16,8	20	stat.	con.	ext.	-

Table 1.2: Existing flywheel energy storage solutions

[a] Ceramic ball bearing with permanent magnet axial thrust reduction
[b] Internal rotor with external flywheel
[c] L3 Communications - Magnet Motoren
[d] High temperature superconducting magnetic bearing
[e] Piller Power Systems
[f] Pentadyne Power Corporation
[g] Trinity Power Corporation

Chapter 2

Basic Theory

2.1 Earnshaws Therorem

The English physicist and mathematician Samuel Earnshaw (1805 - 1888) stated the Earnshaw Theorem in the year of 1842. It says that an object cannot be levitated freely and be stabilized by a static magnetic field. The Theorem can also be concluded by the later postulated Maxwell Equations.

2.1.1 Explanation

For an object levitated in a stable equilibrium by a static magnetic field, perturbations in any direction should not break the equilibrium and the object should fall back into its original position. All surrounding force vector elements, caused by a static magnetic field, should point towards the stable point. This is simply not possible.

$$\int_{\Gamma} \vec{F} \mathrm{d}\Gamma = \int_{\Omega} \mathrm{div}\left(\vec{F}\right) \mathrm{d}\Omega \tag{2.1}$$

The Gauss' Theorem, see equation 2.1, says that the integral of the radial component of the force $\vec{F}$ over the surface Γ must be equal to the integral of the divergence of the force $\vec{F}$ over the concluded volume Ω. This means a stable equilibrium requires a static magnetic field, that causes a vectorial force $\vec{F}$ that points towards the stable point from all directions. Therefore the surface integral over $\vec{F}$ would be different from zero which does not satisfy the Laplace Equation.

Earnshaw proved that for a levitating object, there always is at least one direction, in which the object cannot be restored into its initial position.

2.1.2 Exceptions

Earnshaw's Theorem is only relevant in classical physics which excludes quantum physics. The following list shows ways around the assumption.

- Diamagnetism: Earnshaw's Theorem does not apply to diamagnetics. External magnetic fields induce eddy currents which cancel the external magnetic field. Superconductors behave like perfect diamagnetic material. When an external magnetic field is applied, induced eddy currents flow resistless through the superconductor and produce a magnetic field that cancels the external field completely. The value of the induced field is exactly equal and opposite in direction to the applied magnetic field.

  For instance a permanent magnet placed above a super conductor is levitating in a stable equilibrium. High temperature superconductors at a temperature of -170°C are arranged relatively easily with dry ice or liquid hydrogen.

- Oscillating fields: An oscillating magnetic field applied to conducting material induces circular alternating currents. This results in diamagnetic behavior of conductive material (usually copper and aluminum) due to Lenz's Law. Repulsive effects and even levitation can be realized with oscillating magnetic fields.

  For instance the Japanese train project "JR-Maglev" levitates at speeds above $150 km/h$ using this effect.

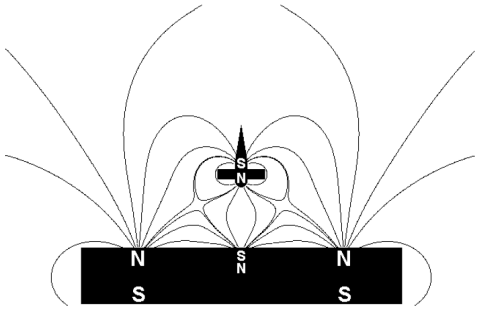

Figure 2.1: Basic concept of the famous toy "levitron" [9]

- Rotation: Spin stabilized magnetic levitation is possible but within certain restrictions. The parameter space for stable levitation is very small. The basic concept in Fig. 2.1 shows a permanent magnet base plate consisting of an outer axial magnetized ring and a permanent magnet rod in the center. The rotating permanent

magnet gyroscope is placed on top. The stabilizing force of the levitating permanent magnet rotor, which keeps it from flipping over, is produced by the gyroscopic force. The gyroscope is levitating in its idle state where the repulsing force of the outer magnet ring and the attractive force of the inner magnet rod equal each other. Of course there is a minimum critical rotating speed for the gyroscope to remain in its stable equilibrium. An interesting fact is that there is a maximum rotational speed as well. [15]

To start the "game", the gyroscope is twisted on a board placed on top of the base plate. When the gyroscope is spinning at the center position the board is carefully lifted up until the gyroscope starts to levitate.

- Ferrofluids: A ferrofluid is a fluid that contains chemically suspended iron-oxide ferromagnetic particles. The interaction between a permanent magnet and the magnetic fluid can be used to stabilize or levitate objects. For instance, a permanent magnet, submerged into a ferrofluid, seeks into a stable equilibrium. A restoring force occurs when the magnet is displaced, however the load capacity is minimal. The ferrofluid's drag on rotation due to its viscosity limits spinning applications.

- Feedback: If the distance between the levitating object and an actuator is measureable and the strength of the electro magnet is adjustable, a stable equilibrium can be achieved with a feedback control system. This is the most common way to circumvent Earnshaw's Theorem. An adjustable electro magnet is in principle comparable to a moving magnet, which is not included in Earnshaw's Theorem either.

2.2 Bearing Components

Basically there are two kinds of bearing components for magnetic bearings or active magnetic bearings. The first one is the "radial bearing" that has to supply forces in radial directions. This bearing type can handle two degrees of freedom and there are two basic implementation types - "homopolar radial bearings" and "heteropolar radial bearings" - which are explained in chapter 4. The second component is the "thrust bearing" which supplies axial forces. With two radial bearing components and one thrust bearing component a complete magnetic bearing system can handle five of the rotor's six degrees of freedom. The remaining 6^{th} degree is rotation around its axis.

2.3 Basic Control Loop

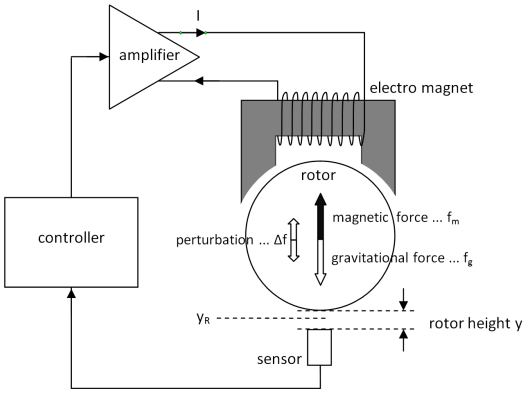

Figure 2.2: Basic active magnetic bearing feedback control loop

Figure 2.2 depicts all basic components of a standard active magnetic bearing system. In the following paragraphs, these elements and their functionalities are briefly described.

The rotor is supposed to be levitated freely and contactless at a certain distance y_R from the bearing's electro magnet. A contactless displacement sensor measures the distance y between the flywheel's rotor and the bearing's electro magnet and feeds the information to the digital controller. Stabilizing the rotor at the nominal position y_R is achieved by compensating the gravitational force $f_g = m \cdot g$ with the magnetic force f_m. Counteracting external perturbation, caused by movement or internal perturbation caused by imbalance (Δf), is desired.

Based on a control scheme, the digital controller sends out a control current signal to the power amplifier. The amplifier supplies the amplified control signal which induces an electric current that is sent through the coil of the electro magnet. The produced magnetic flux flows through the iron core of the electromagnet and spreads through the air gap into the rotor.

This simplification in Fig. 2.2 of an active magnetic bearing shows just one degree of freedom. A complete magnetic bearing system needs at least three control loops to establish a stable equilibrium and a contactless levitation.

Chapter 3

The Amplifier

The amplifier that was used is a push-pull class AB amplifier with a maximum voltage of ± 20 Volts and a maximum surge current of ± 3.8 Ampere and a maximum continuous current of ± 2.8 Ampere. The cut-off frequency is above 50 kHz which is enough for the PID control, operated at 16 kHz, and state space control, operated at 1 kHz.

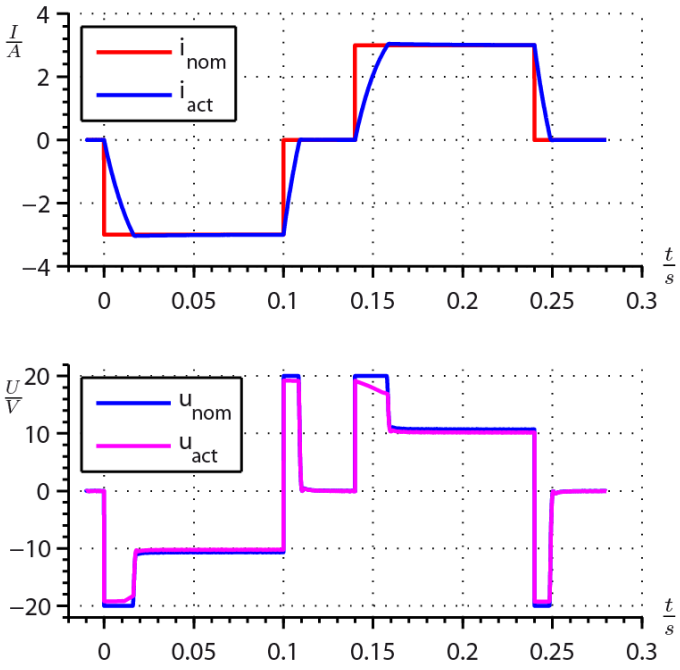

Figure 3.1: Maximum positive and negative control current

Figure 3.1 shows the performance of the amplifier with an integrating current controller designed by frequency response analysis. The maximum current slope is 325 Ampere per

second which occurs when the controller tries to reduce the maximum current to zero as fast as possible and therefore applies the maximum negative voltage to the ohmic inductive load.

An interesting fact that can be seen in figure 3.1 is that the rise time from 0 to -3 Ampere is significantly shorter than the rise time from 0 to $+3$ Ampere.

Chapter 4

The Electro Magnet

The electro magnet is the active component of the control loop and has to produce the attractive force to stabilize the rotor. It is desired to produce as much force as possible with a minimum of power. Therefore reducing the air gap results in a higher level of efficiency. In contrast the construction and measurement of the displacement gets more difficult. To produce as much force as possible, a material that can conduct as much flux density as possible without saturating is used.

The major standby losses of an evacuated high-speed flywheel energy storage, no matter if loaded or not, are the electromagnet components. For PM[1] biased magnetic bearings the standby losses can be further decreased.

4.1 Magnetic Bearing Components

Basically there are two different kinds of bearing components used in magnetic bearings. The radial bearing which can handle two degrees of freedom ($x,\ y$) and has to stabilize the rotor in radial directions and the thrust bearing which has to compensate forces in axial directions (z).

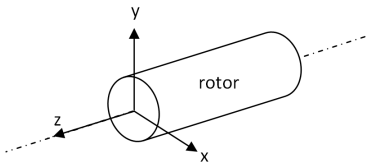

Figure 4.1: Radial and axial directions

[1] Permanent magnet

In static applications the orientation of the axis determines which bearing component has to bear the static gravitational load additionally. A vertically aligned axis increases the thrust load and a horizontally aligned axis increases the radial load in one direction. This can be inappropriate for hetero-polar radial bearings. A possible way to reduce standby power is to compensate the static load with permanent magnets. This bearing type is called PM biased AMB.

Radial electro magnets can be arranged in two different configurations, which are homopolar and heteropolar. Fig. 4.2 shows that the radial electro magnets are all mounted on a single piece of iron. A big advantage of the heteropolar arrangement is the narrow design, that allows a shorter rotor which increases flexible mode frequencies. Furthermore, the radial bearing can be manufactured similarly to electric motors which helps reducing the costs. A major disadvantage is that a single point on the rotor's surface observes four changes in polarity of the magnetic field during one single rotation. This leads to significantly increased hysteresis losses and eddy current iron losses with increased rotational speeds.

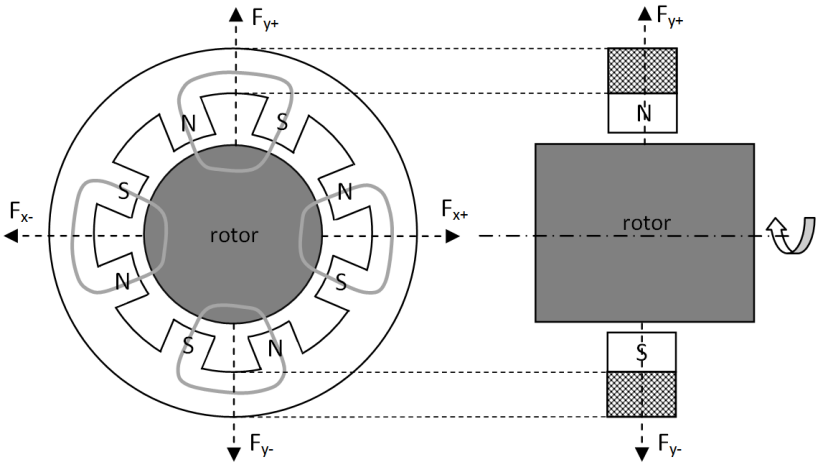

Figure 4.2: Heteropolar radial bearing configuration [19]

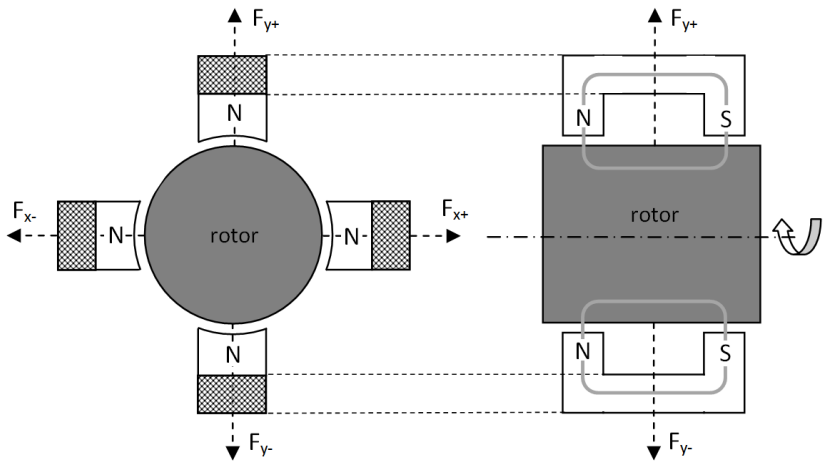

Figure 4.3: Homopolar radial bearing configuration [19]

As shown in figure 4.3 the magnetic field lines of the radial electro magnets are parallel to the rotor's rotational axis. This configuration is called homopolar. A single point on the rotor's surface observes just a variation in field intensity of the radial bearing's magnetic field during one rotation. The advantage of this configuration is a substantial reduction of rotational eddy current iron losses.[19]

High speed flywheels are levitated in an evacuated housing and therefore the rotor's only possible heat dissipation is radiation. Hence this configuration is a critical design criteria. A disadvantage is the broader design which increases the rotor's length which subsequently leads to lower flexible mode frequencies. Another disadvantage is that the radial bearing's electro magnets consist of several single iron cores which increases costs and complicates construction.

4.2 Magnetic Force

Thanks to numerical multi-physics simulation software, exact analysis of iron loops are possible. Nevertheless an analytical approximation helps to define the necessary electrical and geometric characteristics roughly. For the following analytical approximation a few assumptions have to be made.

- The magnetic flux runs entirely through the iron and the air gap volume. This means the leakage flux in the surrounding air is neglected.
- The iron cross section A_{fe} is constant along the entire magnetic circuit. This simplifies computation of the iron resistance, because edges and corners are not taken into account.

- The air gap cross section is equal to the iron cross section. This means that the whole magnetic field is homogeneous in the iron and the air gap, as shown in figure 4.4.

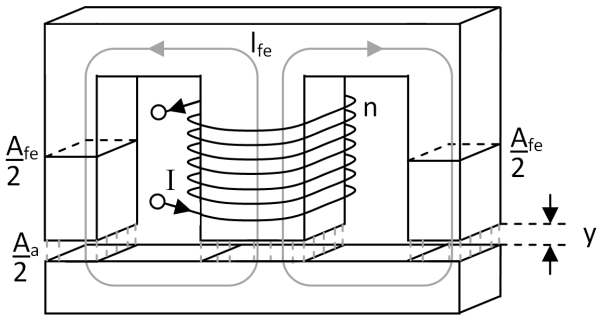

Figure 4.4: E-core electro magnet

Figure 4.4 shows an E-core electro magnet with the average iron length l_{fe}, average iron cross section A_{fe}, average air cross-section A_a, current I, number of windings n and the air gap y.

$$\oint \underline{\mathbf{H}} \cdot d\underline{\mathbf{s}} = l_{fe} \cdot H_{fe} + 2 \cdot y \cdot H_a = n \cdot I = \Phi \tag{4.1}$$

$n \cdot I$ is often called the magnetomotive force. Considering that $B = \mu_0 \cdot \mu_R \cdot H$ and remembering the assumption that $B_{fe} = B_a$, equation 4.1 can be enhanced.

$$l_{fe} \frac{B}{\mu_0 \cdot \mu_R} + 2 \cdot y \cdot \frac{B}{\mu_0} = n \cdot I \tag{4.2}$$

$$B = \mu_0 \frac{n \cdot I}{\left(\frac{l_{fe}}{\mu_R} + 2 \cdot y\right)} \tag{4.3}$$

The attraction force of electro magnets is generated at boundaries between differing permeability $\mu = \mu_0 \cdot \mu_R$. The calculation of the force is based on the partial derivative of the field energy by using the principle of virtual displacement [19]. In equation 4.4 W_a is the energy stored by the volume of the air gap.

$$W_a = \frac{1}{2} B_a H_a A_a \cdot 2 \cdot y \tag{4.4}$$

$$f = -\frac{\partial W_a}{\partial y} \tag{4.5}$$

Inserting equation 4.4 into eq. 4.5 results in

$$f = \frac{B_a^2 A_a}{\mu_0} \tag{4.6}$$

Inserting eq. 4.3 into eq. 4.6 provides a good approximation for f.

$$f = \mu_0 \left(\frac{n \cdot I}{\frac{l_{fe}}{\mu_R} + 2 \cdot y} \right)^2 A_a \tag{4.7}$$

To enhance results from equation 4.7 the relative permeability μ_R can be obtained from a B-H diagram that belongs to the properties of the used material.

4.3 Dimensioning

To start from scratch the primarily feature is to generate a maximum force f_{max} with the amplifier's maximum current I_{max}. For a given amplifier's maximum current and demanded maximum force at the nominal displacement y_R, the number of turns neglecting the iron is easy to calculate.

From the number of turns n and I_{max} the necessary iron cross section run through by the magnetomotive force $\Phi = n \cdot I = B \cdot A$ can be derived. A useful iron cross section of the journal, that does not cause too much saturation, determines the coil bobbin's inner dimensions. E.g. in figure 4.5 an average magnetic flux density of 1.5 Tesla for standard sheeted steel should not be exceeded, since a further increase of the magnetic field results in a relatively small increase of magnetic flux.

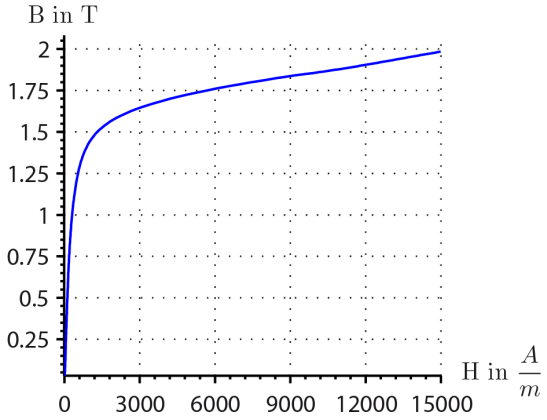

Figure 4.5: B-H diagram of sheeted steel

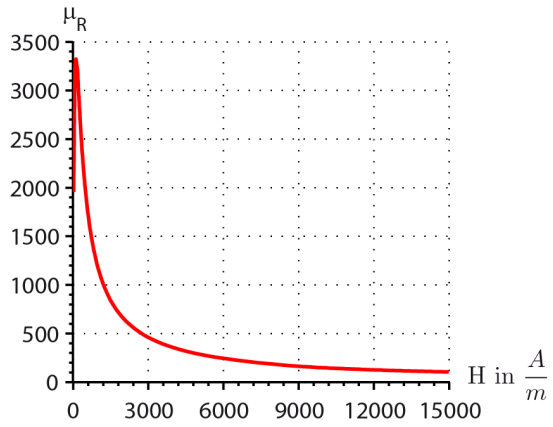

Figure 4.6: Relative permeability μ_R extracted from Fig. 4.5

The next step is to calculate the coil's cross section A_w, the average winding length lw, the total length of the enameled copper wire l_{co} and the coil resistance R. The coil cross section is calculated with the fill factor F that expresses the ratio of the coil winding's cross sectional area and the required space.

$$F = \frac{d_w \frac{\pi}{4} \cdot n}{a_w \cdot b_w}, \qquad \cdots \qquad F < 1 \tag{4.8}$$

Unless the coil's winding is not orthocyclically, which would result in a perfect fill factor F, a good approximation for a so-called "wild winding" is given in eq. 4.9. This is the ratio between the wire cross section and the surrounding rectangular box.

$$F_{wild} \approx \frac{d_w^2 \frac{\pi}{4}}{d_w^2} = \frac{\pi}{4} \tag{4.9}$$

Independently from the ratio of the coils width a_w and the coils height b_w, the average winding length l_w can be estimated by equation 4.10.

$$l_w = 4 \cdot \left(\sqrt{A_{fe}} + \sqrt{A_w} \right) \tag{4.10}$$

With the estimated fill factor F_{wild} from equation 4.9 the coil's cross section A_w and the total copper wire length l_{cu} can be calculated with equation 4.11 and 4.12.

$$A_w = d_w^2 \cdot n \tag{4.11}$$

$$l_{cu} = l_w \cdot n \tag{4.12}$$

With the copper wire's specific resistance ρ the coil's total ohmic resistance R can be estimated with equation 4.13.

$$R = l_{cu} \cdot \rho \tag{4.13}$$

Further, the necessary maximum dc-voltage $U_{max} = R \cdot I_{max}$ to run the maximum DC-current I_{max} through the coil and corresponding maximum power dissipation $P_{max} = \frac{U_{max}^2}{R} = I_{max}^2 \cdot R$ can be calculated. To ensure high dynamic control, the amplifiers maximum DC-voltage U_{max} should be a multiple of the nominal DC-voltage $U_R = R \cdot I_R$ to overcome the inductance as fast a possible. The nominal current I_R is the required current to compensate the gravitational force. An estimation for the possible inductance L is given in equation 4.14.

$$L = \frac{n^2 \cdot \mu_0 \cdot \mu_R \cdot A_w}{l_{fe}} \tag{4.14}$$

The average iron length l_{fe} is used in equation 4.14 as average flux line length. Hence the time constant of the electro magnet can be expressed.

$$\tau = \frac{L}{R} \tag{4.15}$$

Since the relative permeability $\mu_R = f(y, I)$ is a function of the magnetic field H, caused by the current I and the rotor displacement y, the results for L and τ are a rough guide.

4.4 Winding

Since copper wire is available in many different diameters, the question is:
"Which is the right one?". In fact, the electro magnet's dynamic behavior τ and it's power consumption P are independent from the wire's diameter as long as the same magnetomotive force $(n \cdot I)$ is run through the iron. The selective criteria is a suitable resistance that fits the amplifiers properties.

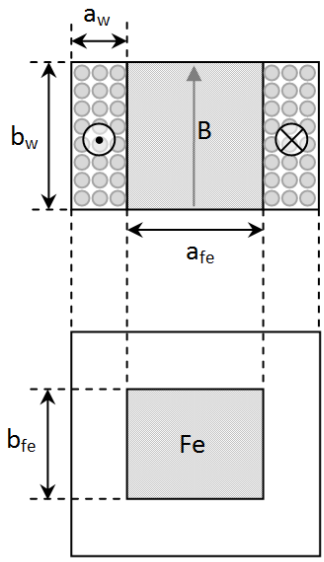

Figure 4.7: Iron and coil cross sections

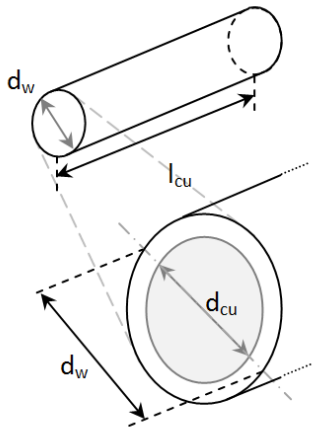

Figure 4.8: Inner and outer diameter of enameled copper wire

#	d_{cu}	d_w	A_{cu}	cu	$lacquer$	m'	ρ
	mm	mm	mm^2	%	%	g m^{-1}	Ω m^{-1}
1	0.03	0.032	0.0007	87.9	12.1	0.006	24.2
2	0.036	0.038	0.001	89.8	10.2	0.01	16.8
3	0.045	0.048	0.0016	89.8	10.2	0.02	10.8
4	0.112	0.116	0.0099	93.2	6.8	0.09	1.74
5	0.14	0.145	0.0154	93.2	6.8	0.14	1.11
6	0.2	0.206	0.0314	94.2	5.8	0.29	0.544
7	0.3	0.308	0.0707	95.2	4.8	0.65	0.242
8	0.355	0.364	0.099	95.4	4.6	0.9	0.173
9	0.4	0.409	0.125	95.6	4.4	1.15	0.136
10	0.5	0.51	0.194	96.1	3.9	1.79	0.087
11	0.65	0.662	0.332	96.4	3.6	2.97	0.052
12	0.8	0.813	0.503	96.9	3.1	4.54	0.034
13	0.95	0.964	0.709	97.1	2.9	6.37	0.0243
14	1.0	1.014	0.786	97.3	2.7	7.04	0.022
15	1.06	1.075	0.883	97.2	2.8	7.88	0.0195
16	1.12	1.135	0.985	97.4	2.6	8.92	0.0175
17	1.18	1.196	1.094	97.4	2.6	9.8	0.0158
18	1.25	1.266	1.227	97.6	2.4	10.99	0.0141
19	1.32	1.336	1.369	97.6	2.4	12.34	0.0126

Table 4.1: 19 different copper wires in comparison [5]

Tabular 4.1 lists 19 different copper wires, sorted by the wire's copper diameter d_{cu}. d_w is the copper diameter, A_{cu} is the copper wire's cross section area, m' is the specific weight and ρ is the specific resistance.

With varying wire diameter d_w and constant magnetomotive force $n \cdot I$, the coil's cross section area A_w slightly varies because the smaller the wire diameter d_w, the more lacquer is built into the coil. Table 4.1 shows the percentage by volume of lacquer and copper for 19 different copper wires. According to the maxim "the more diameter, the better", the coil's cross section area A_w and the average iron length l_{fe} decrease slightly, which increases the force f. Another positive fact is that an orthocyclically winding is easier to achieve for thicker wires and they can be coiled significantly faster. A disadvantage of thicker wires though is their lack of flexibility which is critical for the first layers of wire on a rectangular shaped journal.

4.4.1 Example

This example features a given sheeted iron core as seen in figure 4.9. The core was taken from an EI-core transformer. The task is to find the appropriate winding properties to match the amplifiers I_{max} and U_{max} and to produce the desired force $f_{max} = m \cdot a_{max}$ where a_{max} is the maximum acceleration and m is the rotor weight.

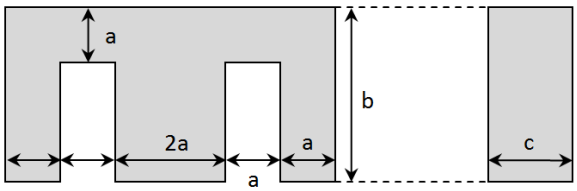

Figure 4.9: Sheeted transformer EI- core:
$(a = 13\text{mm}, b = 51\text{mm}, c = 27\text{mm})$

$$l_{fe} = (2 \cdot a + b) \cdot 2 = (2 \cdot 13\text{mm} + 51\text{mm}) \cdot 2 = 154mm = 0.154m \tag{4.16}$$

$$A_{fe} = 2 \cdot a \cdot c = 2 \cdot 13\text{mm} \cdot 27\text{mm} = 702\text{mm}^2 = 7.02\text{cm}^2 \tag{4.17}$$

The maximum number of coil windings is calculated. Then the maximum magnetic force f_{max}, the maximum flux density B_{max}, the power dissipation P_{max}, the current density J_{max} and the necessary dc-voltage U_{max} for the maximum current $I_{max} = 2.8$ Ampere are determined. Tabular 4.2 also shows the copper cross section A_{cu} and the wire diameter d_w.

#	d_w	A_{cu}	f_{max}	B	P_{max}	J	U_{max}	n	R	L	τ
	mm	mm^2	N	T	W	$A \cdot mm^{-2}$	V		Ω	mH	ms
1	0.65	0.28	42	0.27	58	9.9	20.7	781	7.4	53	7.3
2	0.75	0.38	24	0.20	32	7.3	11.6	583	4.1	30	7.3
3	0.78	0.39	20	0.19	27	7.1	9.6	524	3.4	26	7.6
4	0.86	0.50	14	0.16	19	5.6	6.8	451	2.4	18	7.3
5	1.00	0.71	7	0.11	10	4.0	3.5	322	1.2	9	7.4

Table 4.2: 5 appropriate wire diameters in comparison

As one can see, wire diameter number three in tabular 4.2 fits the amplifier's properties best. With the maximum current $I_{max} = 2.8$A the electro magnet still causes enough force at a distance of five millimeters. The result in equation 4.18 is calculated using equation 4.7. The corresponding μ_R is extracted from the data which figure 4.6 is based on.

$$f_{max} = 4\pi \cdot \left(\frac{518 \cdot 2.8}{\frac{0.154}{700} + 2 \cdot 5 \cdot 10^{-3}} \right)^2 \cdot 7.02 \cdot 10^{-4} = 17.7 \text{ N} \tag{4.18}$$

The most important fact is that only half of the maximum voltage of the amplifier is necessary to drive the maximum current. The standby current I_R to compensate the gravitational static load, is 0.52 Ampere, see chapter 6. The standby voltage $U_R = R \cdot I_R$ and therefore $U_R = 0.52\ A \cdot 3.4\ \Omega = 1.77\ V$. This is less than a tenth of the amplifier's maximum voltage and allows fast current changes to counteract external perturbation. The estimated number of turns ($n_{est} = 524$) from tabular 4.2 complies to the actual winding that was built into the EI iron core ($n_{act} = 518$). The magnetic flux density of wire number three in tabular 4.2 shows that the sheeted iron is far from being saturated. The current density at maximum current is not critical either. Since this current is only expected to occur for short periods of time, current densities weigh above 10 $A \cdot\ mm^{-2}$ are acceptable.

Chapter 5

Displacement Measurement

The contactless measurement of the rotor's displacement from the initial position y_R has several requirements to fulfill. The range of measurement is $0 \leftrightarrow \ 2 \cdot y_R$ assuming y_R in the middle of the maximum air gap. The output shall be a linear voltage signal that represents the absolute position of the rotor.

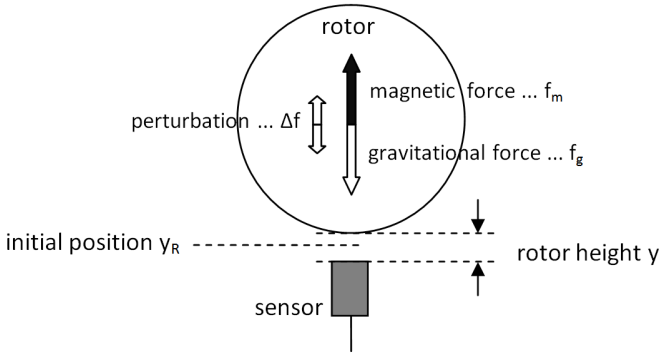

Figure 5.1: Sensor and rotor from the basic control loop in section 2.3

Immunity against static and alternating magnetic fields is obligatory. Since the control system operates at a specific sampling rate, the dynamic behavior and accuracy have to meet the specifications. The dynamic requirements are determined by the occurring perturbation in action. This includes external forces evoked by movement and vibration as well as internal forces due to the rotor's unbalance. Based on the rotor's critical bending speed the maximum rotational speed provides an upper limit. Further the system has to be insensitive to cracks, scratches and any other rough surface deviation. For operation in evacuated environment the displacement measurement must be unaffected by negative pressure and oil vapor. The measuring system for the radial bearing component additionally has to be insensitive to the axle's round shape.

5.1 Possible Measurement Methods

5.1.1 Optical Measurement

Optical measurement methods provide both, a high accuracy down to the sub-micrometer range and a high bandwidth of measureable rotor deviation. With immunity against electromagnetic fields this method is clearly state of the art for static active magnetic bearing systems. Potential problems with dust and condensing oil vapor in the rough environment of an evacuated high-speed flywheel is the knock-out criteria for optical measurement methods. However, if oil vapor is avoidable, there still is the risk of small particles breaking off the rotor lamination. If an exceptionally external force occurs during the operation, like a small fender bender or an overlooked speed bump, the rotor could get in contact with the emergency tough-down bearing. An incident like this would, of course, produce dust. The still functional flywheel could get inoperative just because of contaminated optical components.

This obvious disadvantage is not an insurmountable obstacle. If, for any reason, alternating electromagnetic fields knock out the following electrical competitors, the major disadvantage, susceptibility of dust, could be compensated for instance with a cleaning system. The target area of the rotor has to be machined precisely and needs a polished finish to establish a continuous reflection. One single scratch or crack could produce active vibration proportional to the rotational speed. There are basically two kinds of possible optical measurement methods.

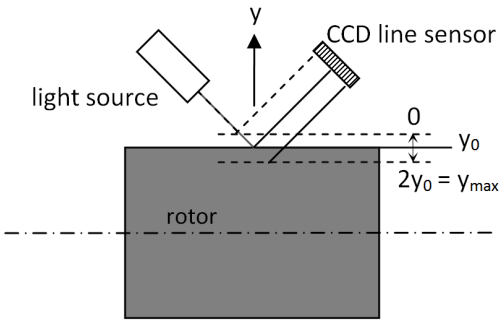

Figure 5.2: Basic laser triangulation measurement

Laser Triangulation Figure 5.2 shows the method in principle. This is the classical industrial setup, without optical aids like lenses. The round surface slightly turns the reflection plane when the rotor is not centered. Therefore a linearization is mandatory. An alternative to a laser light source would be a spot light source having a surface of

a predetermined irradiation area. Therefore the measurement system has to track an illuminated area on the CCD[1] line instead of a point. This modification is more stable to surface roughness.

Generally CCD sensor lines can be read fast enough to fit the dynamic specifications. The accuracy is depending on the number of pixels built into the CCD line as well as the surface quality and the light source.

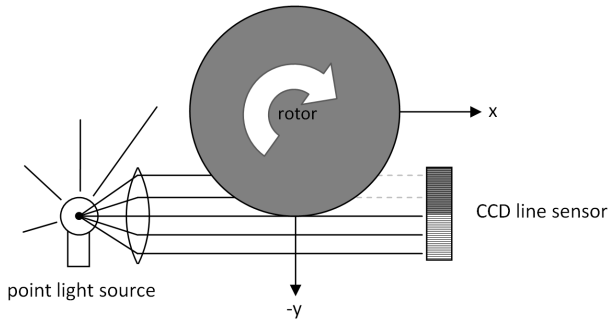

Figure 5.3: Principle of light barrier measurement

Light Barrier Principle Figure 5.3 shows the basic setup. An improvement would be one light source radiating at a 45° angle feeding two orthogonal arranged CCD lines for the x and y displacement. This method needs a lot of free space and has relatively large optical paths and is therefore not acceptable for compact mobile applications.

5.1.2 Capacitive Measurement

This method also provides high accuracy down to the sub-micrometer range combined with high dynamics and immunity against alternating electromagnetic fields. Influences of dust and oil is an issue though. For instance the relative permittivity ϵ_R of vacuum is 1. In comparison ϵ_R of oil is $\approx 2.5 \ldots 5$ and ϵ_R of water is ≈ 80.

Figure 5.4 shows a typical capacitive measurement electrode. The inner electrode and the outer protecting ring are of the same electrical potential. The protection ring is used to provide a homogenous field which is essential to resolve the distance as linear as possible.

A much more complicated issue is the radial bearing component. A minimum of two displacement sensors x and y measuring simultaneously are required. The conductive

[1] Charged couples device

rotor which can be interpreted as a floating electrode is connecting both capacities of the x-channel and the y-channel. A possible workaround would be mounting two electrical isolated target rings on the rotor. This complicates the manufacturing process and increases costs.

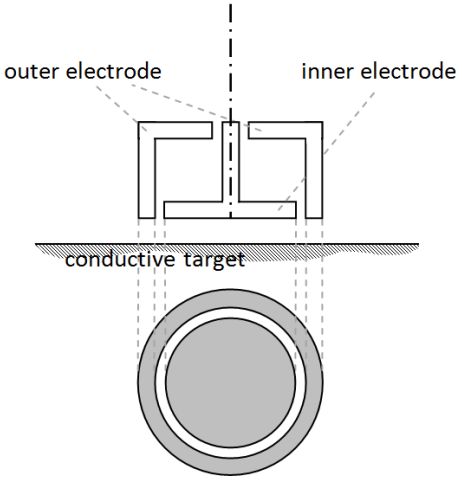

Figure 5.4: Basic capacitive displacement measurement sensor setup

5.1.3 Inductive Measurement

High accuracy down to the micrometer range and high dynamics are achievable. Magnetic fields are not influenced by dust and oil because the relative permeability μ_R of vacuum is the same as the relative permeability of oil and water.

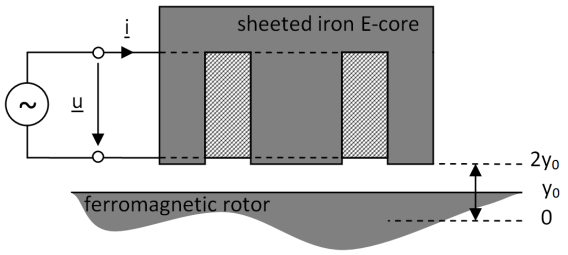

Figure 5.5: Inductive Measurement

Since the inductance L cannot be measured directly, there are two basic methods to measure the inductance:

(a) An oscillating R-L-C circle, where a change in inductance is proportional to the

change in the oscillating circle's resonance frequency.

(b) Current- and voltage-sensing, where the inductance can be calculated from the inductance's voltage and current signal.

The disadvantages are discussed further in section 5.2.

5.1.4 Eddy Current Measurement

The geometric structure is very similar to the inductive measurement. Instead of the sheeted iron core a ferrite core is used to enable higher measurement frequencies.

The fundamental difference between the inductive measurement and the eddy current measurement is the cause of a variation in inductance. The change of inductance measured with inductive measurement is caused by altering the ferromagnetic target's geometry that leads to a different distribution of the magnetic flux lines and therefore alters the magnetic properties of the iron loop. An approximation of the rotor to the inductive sensor therefore leads to an increase of inductance.

The eddy current measurement in contrast measures the amount of induced eddy currents in an electrical conductive target. The induced eddy currents weaken the sensor's initial magnetic field due to Lenz's Law and therefore an approximation of the rotor towards the eddy current sensor cancels the field even further. The increasing cancellation of the sensor's alternating magnetic field is measured as a reduction of the initial inductance.

5.2 First Experiment - Inductive Measurement

The first attempt to build up a measurement system was based on method (b) from subsection 5.1.3.

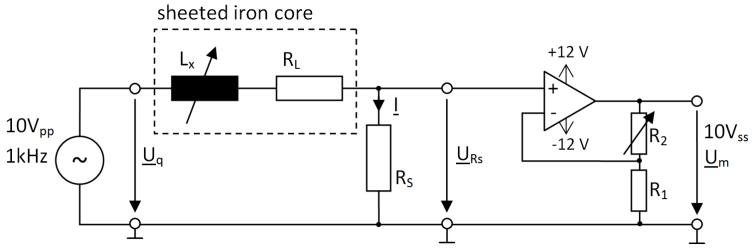

Figure 5.6: Circuit for the displacement measurement with inductive iron core sensor

To supply the 1kHz sinusoidal 10 V_{pp} voltage $\underline{U}_q$ from figure 5.6 the "HAMEG Arbitrary Function Generator HMF2550" was used. The winding on the iron core, represented by the variable inductance L_x and the associated ohmic resistor R_L, is fed by the voltage source. The resulting current is measured by the amplified voltage at the shunt resistor R_S. The HAMEG function generator keeps the source voltage constant although the complex resistance varies due to rotor displacement. Since the "dSpace Ds 2002 ADC[2] Board" can operate at $\pm 5\ V$ or $\pm 10\ V$, the shunt's current signal is amplified to 10 V_{pp}.

To set up a wound sheeted iron core, the smallest available transformer with a two-piece welded iron core was used. Milling one millimeter into the weld separated the E-core piece from the corresponding I-bar piece. Although the weld was milled, it still holds the iron sheets well together.

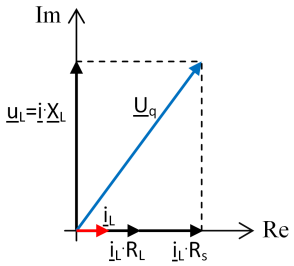

Figure 5.7: Corresponding vector diagram

The amplified current signal divided by the amplification and divided by R_s implies the vector $\underline{i}_L$. The signal $\underline{U}_q$ subtracted with $\underline{i}_L \cdot R_s$ and subtracted with $\underline{i}_L \cdot R_L$ implies the vector $\underline{u}_L$. With the frequency f, the inductance can now be calculated by $\underline{u}_L$ divided by $\underline{i}_L$ which is $\underline{X}_L$.

$$L_x = \frac{\underline{X}_L}{j \cdot 2\pi \cdot f} \tag{5.1}$$

It is possible to calculate the inductance L_x based on the RMS[3] values of $\underline{u}_L$ and $\underline{i}_L$ with equation 5.2

$$L_x = \frac{\sqrt{u_L^2 - i_L^2}}{2\pi \cdot f} \tag{5.2}$$

To gain additional information from the current and voltage signal's phase shift, the fast Fourier transformation (FFT) was chosen. The complex values were extracted from the

[2] Analog to digital converter
[3] root mean square

Fourier transformation output vector at the corresponding measurement frequency entry. When the inductance is derived, the rotor position has to be interpolated based on a lookup table, or by a polynomial approximation. This means a direct calculation of L is not necessary and is wasting calculation time. It is sufficient to implement a lookup table from the FFT[4] values of both signals and the corresponding rotor position.

An interesting fact is that an external alternating magnetic field interferes both signal's absolute value relation in opposite direction to the measurement signal's phase difference. Based on this knowledge two different lookup tables were implemented relating the absolute values and the angle of the FFT result to the rotor's position. The independent interpolated position signals were merged to reduce the interference of alternating magnetic fields.

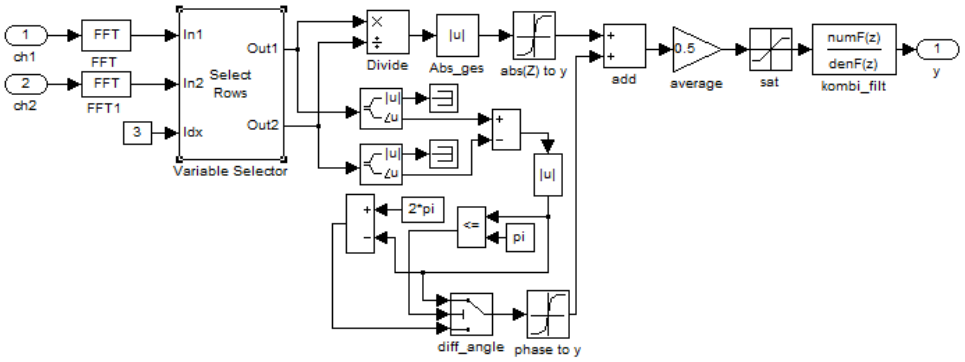

Figure 5.8: Simulink diagram of the measurement signal evaluation

Figure 5.8 shows the two signals "ch1" and "ch2" coming from the dSpace A/D converters fed into the FFT blocks. The samples converted at a sampling frequency f_s of 16 kHz are converted into [16x1] row vectors at 1 kHz before entering this subsystem. The third vector entry is selected because the measurement signal frequency is 2 kHz. Then 2 different lookup tables are used to obtain the position of the rotor. To avoid jumping values of the phase difference due to the angular range of $-\pi$ to π, a compensation block was implemented. The position signal from the absolute value ratio lookup table and the signal from the phase difference lookup table are averaged. The saturation block limits the signal space to the physical possible boundaries. After that a first order LP filter with a cut-off frequency of 150 Hz was used to reduce measurement noise.

Figure 5.9b clearly shows the weakness of the inductive measurement. The measured inductance is varying with a change in the measurement area's geometry and the measurement area's magnetic properties of the material. The rotor's material properties are

[4]Fast Fourier transformation

altered by the bearing's electro magnet due to material saturation. This can be observed in figure 5.9c where the rotor's position is deviated by 0.5 mm although the rotor is fixed. As long as the maximum current is sent through the electro magnet the inductive measured displacement is deviated. Additionally, the measurement iron core's winding is sensitive to fast changes in the electro magnet's current. This alternating stray field flux $\frac{\partial \Phi}{\partial t}$ influences the measurement carrier signal and leads to the perturbation in 5.9b

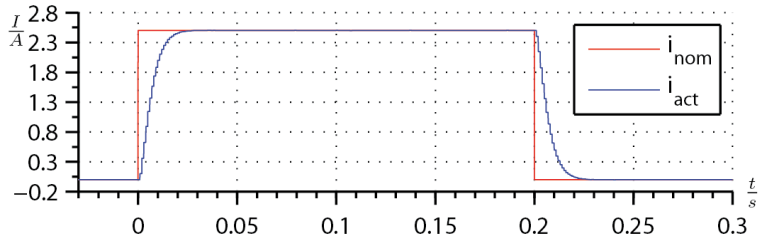

(a) Current of the bearings electro magnet

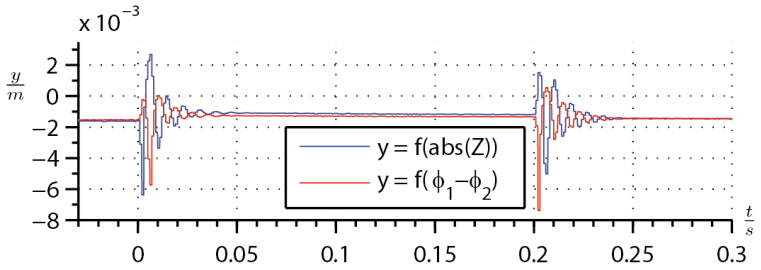

(b) Rotor displacement signals with current interference

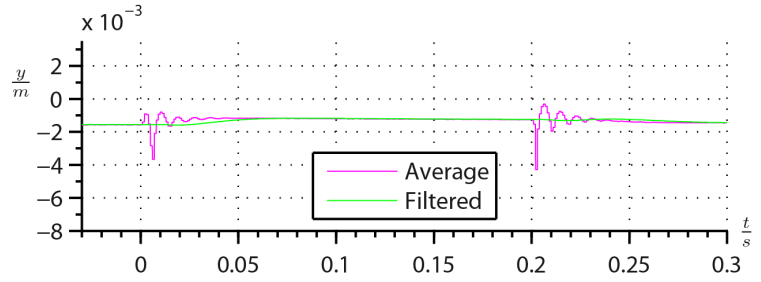

(c) Improvement with averaging and filtering

Figure 5.9: Inductive measurement with "fixed" rotor at 1.5 mm

Digital low pass filtering in the controller's bandwidth is not an elegant solution and causes additional phase shift that deteriorates the controller's performance. In fact the alternating magnetic field perturbation is of low frequency compared to the measurement frequency. Therefore one possible solution is to increase the measuring frequency and cancel induced voltages with active filtering before sampling. Figure 5.10a and 5.10b show the sensitivity of the iron core's resistance and inductance over frequency. The

values for R and L are calculated from the complex impedance of the iron core based on the model $\underline{Z} = R \parallel L$. R represents the ohmic losses and the iron losses which increase dramatically with rising frequency. As one can see in figure 5.10b the sensitivity also decreases dramatically with rising frequency. Therefore increasing the measurement frequency with an iron core is not an option. This leads to the following second experiment in 5.3.

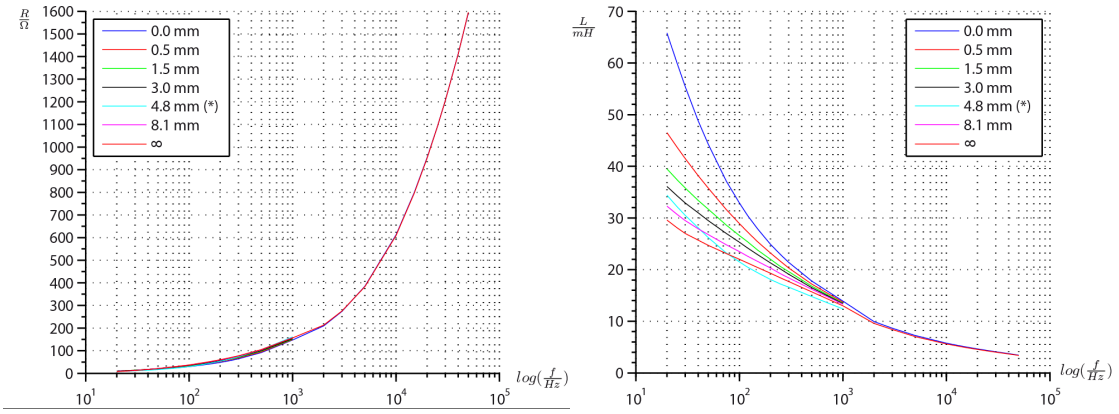

(a) Resistance of the R||L model

(b) Inductance of the R||L

Figure 5.10: Electrical properties of the inductive measurement iron core

5.3 Second Experiment - Eddy Current Measurement

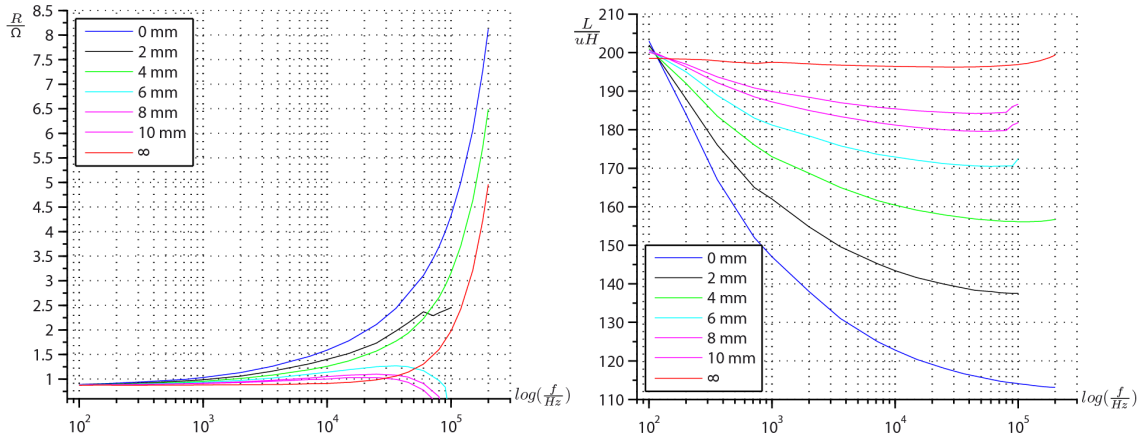

(a) Resistance of the ferrite core

(b) Inductance of the ferrite core

Figure 5.11: Electrical properties of the eddy current measurement ferrite core

As one can clearly see in Fig. 5.11 the inductive behavior over the frequency of the ferrite core is different to the iron in figure 5.10. With increasing frequency the variation in in-

ductance due to rotor displacement increases. If no electric conductive target is available (∞-curve) the inductance remains almost constant. This time the complex impedance $\underline{Z}$ is expressed as R-L serial model. The ohmic resistance R also represent losses in the ferrite material due to polarity change. The curves with 6mm, 8mm and 10mm in figure 5.11a are not realistic and contribute to a measurement error using the HAMEG Programmable LCR Bridge HM 8118.

5.3.1 Functional Principle

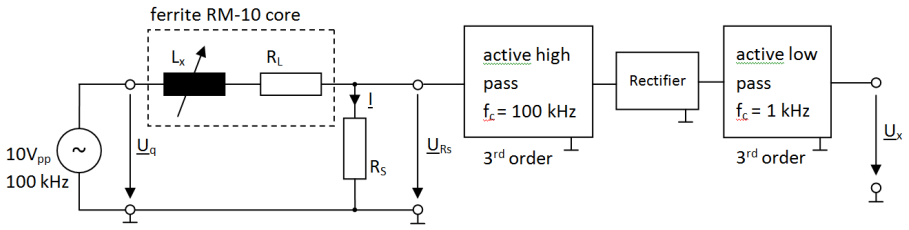

Figure 5.12: Circuit overview of the eddy current measurement system

To set up a prototype of an eddy current measurement system, one half of a RM-10 ferrite core transformer is used. Aluminum was chosen as target material since it features a higher physical strength than copper. The winding of enamelled copper wires with a diameter of 0.05 mm^2 is excited with a sinusoidal 10 V_{pp} signal at 100 kHz supplied by the "Rohde & Schwarz Arbitrary Function Generator AFGA" (1μHz ... 20MHz). Thanks to the high measurement frequency compared to the expected perturbation frequencies the current signal can easily be filtered with higher order active filters. The perturbation from the bearing's electro magnet due to fast current changes cannot be higher than half of the control system's operating frequency. Additionally, the electro magnet's time constant is another limit to fast current changes. A switching amplifier, which is not used, would produce noise at 5 ,10 or 20 kHz. The measurement frequency is almost two decades above the expected interferences. Therefore with a third order active high pass filter almost -120 db attenuation to the interference of alternating electromagnetic fields can be achieved.

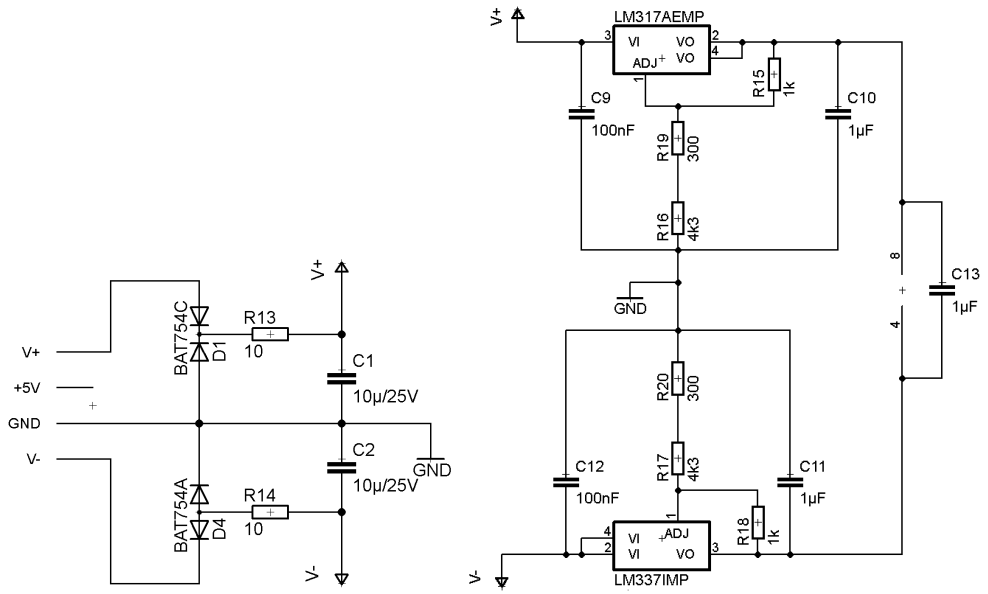

(a) Power connection (b) Linear voltage regulators

Figure 5.13: Power supply for the eddy current measurement board

The circuit in figure 5.13a is connected to a modified PC-power supply which provides $\pm 12\ V$. It features a reverse polarity protection with Schottky diodes and a low pass filter with a cut-off frequency of $f_c = 1.6\ kHz$ for further voltage ripple rejection. The linear positive and negative voltage regulator in figure 5.13b provides $\pm 7\ V$ for the dual supplied low noise amplifier "TLC 2272".

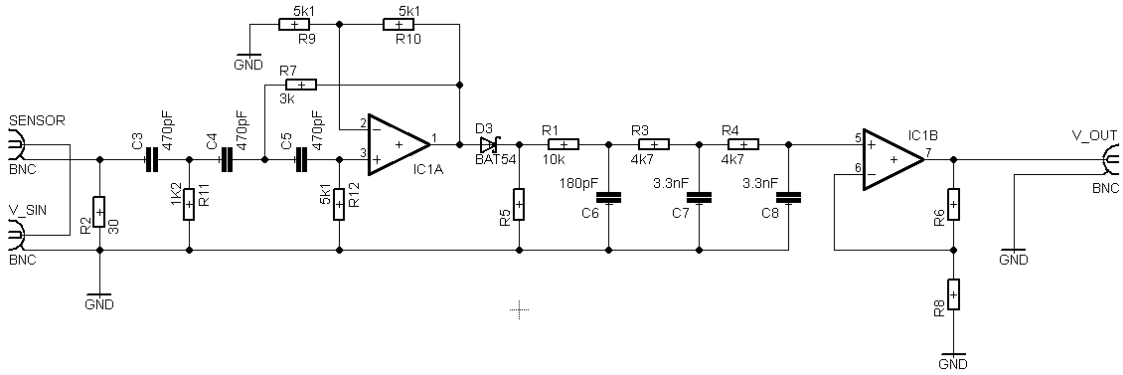

Figure 5.14: Measurement signal converting

On the left side in figure 5.14 one can see the connection to the ferrite core (SENSOR) and to the external sine voltage source (V_SIN). The external voltage source is supplied by the "Rohde & Schwarz Arbitrary Function Generator AFGA".

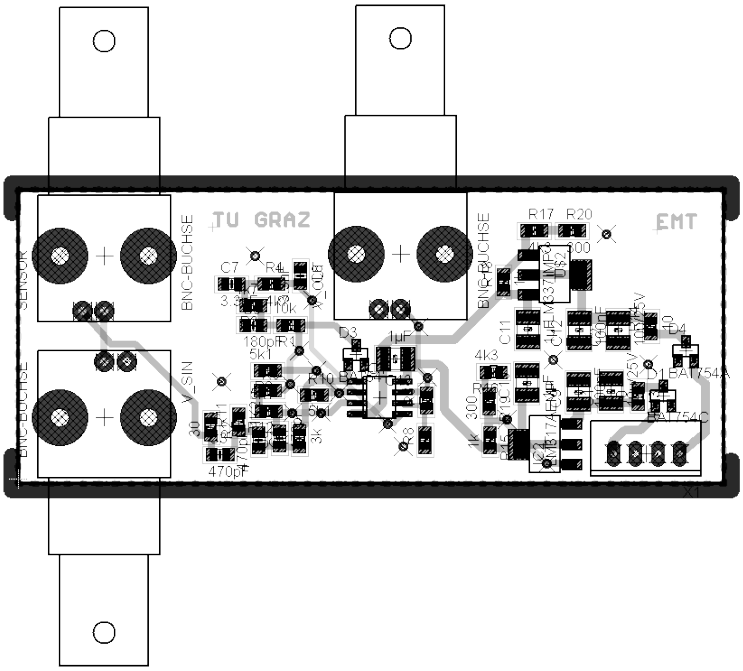

Figure 5.15: Circuit board of the eddy current measurement

The ferrite core is exited at 7.3 V_{pp} at 100 kHz. The current signal is high pass filtered with a third order active Chebyshev I filter with cut-off frequency $f_c = 100\ kHz$. Subsequently the current signal is rectified with a Schottky diode. The discharge resistor to ground and the third order low-pass filter rectify the current signal. After that the DC-voltage is amplified to fit to the ADCs $\pm 5\ V$ maximum input voltage range.

5.3.2 Statistical Properties

The DC output voltage ranges from 3.5 V to 5 V for a rotor displacement from $y = 0$ to approximately 20 mm. The output voltage range covers 15 % of the ADC's maximum DC-voltage range, which means an improvement by the factor of $6.\dot{6}$ is possible with additional voltage level adjustment. One additional bit in quantization resolution results in $-6\ dB$ quantization noise.

$$\text{ld}\ (\frac{10}{1.5}) = 2.737 \tag{5.3}$$

Eq. 5.3 shows that more than two bits are virtually not used and that the quantization noise could be reduced by $-16.5\ dB$ as shown in Eq. 5.4

$$20 \cdot \log\left(\frac{1}{6.\dot{6}}\right) = -16.5\ db \tag{5.4}$$

$$\Delta y = \frac{(y_2 - y_1)}{2^{16} - 1} \cdot \left(\frac{10\ V}{(V_2 - V_1)} \right) \tag{5.5}$$

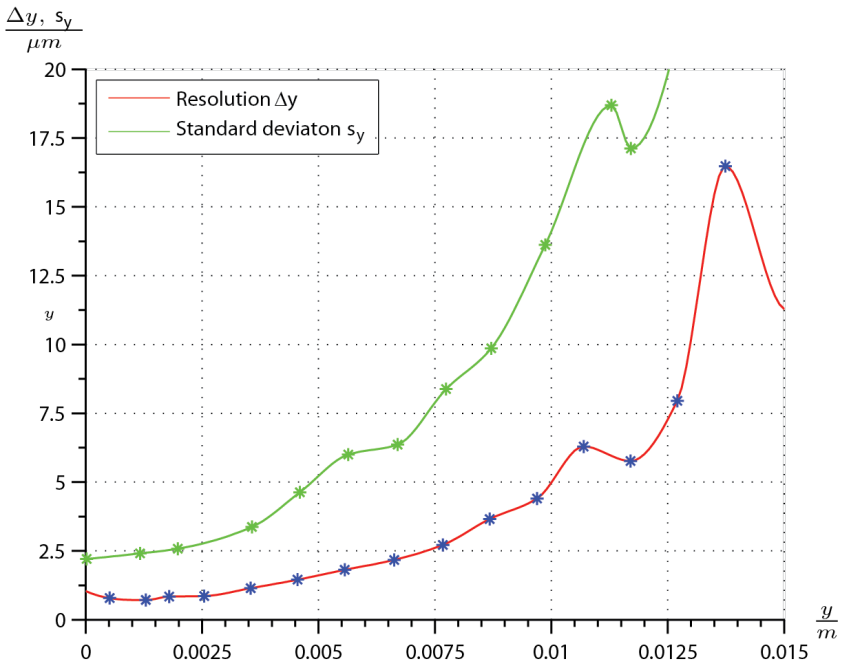

Figure 5.16: Average resolution at the calibration intervals

Figure 5.16 shows the resolution of the air gap Δ_y and the standard deviation s_y of the position signal y of the levitated rotor. The distances where the standard deviation was determined are marked with stars. The stars on the resolution line mark the middle of the evaluated interval. Even though the characteristic curves were determined independently, both the resolution and the standard deviation show an unexpected curse around eleven millimeters, where the uptrend is shortly interrupted by a turn-around. First of all this peculiar point is out of the maximum rotor displacement of 10 mm and second, the measurement intervals are to far apart for more general statements. Tabular 5.1 displays the statistical properties of the displacement measurement. The data is sorted by the measurement points $\overline{y}$. The quantization resolution is Δy and the standard deviation is s_y.

#	$\overline{y}$	Δy	s_y	$2 \cdot s_y$
	mm	μm	μm	μm
1	0.02	1.03	2.21	4.42
2	1.17	0.72	2.41	4.82
3	1.98	0.85	2.58	5.16
4	3.57	1.15	3.37	6.74
5	4.60	1.47	4.63	9.26
6	5.64	1.84	6.00	12.00
7	6.70	2.20	6.36	12.72
8	7.74	2.77	8.38	16.76
9	8.71	3.68	9.86	19.72
10	9.87	4.68	13.62	27.24
11	11.29	5.96	18.69	37.38
12	11.71	5.76	17.12	43.25
13	13.05	10.69	24.11	48.22
14	14.02	15.87	49.60	99.20
15	15.12	11.27	32.86	65.72
16	18.02	29.86	44.36	88.72

Table 5.1: Statistical properties of the eddy current displacement measurement

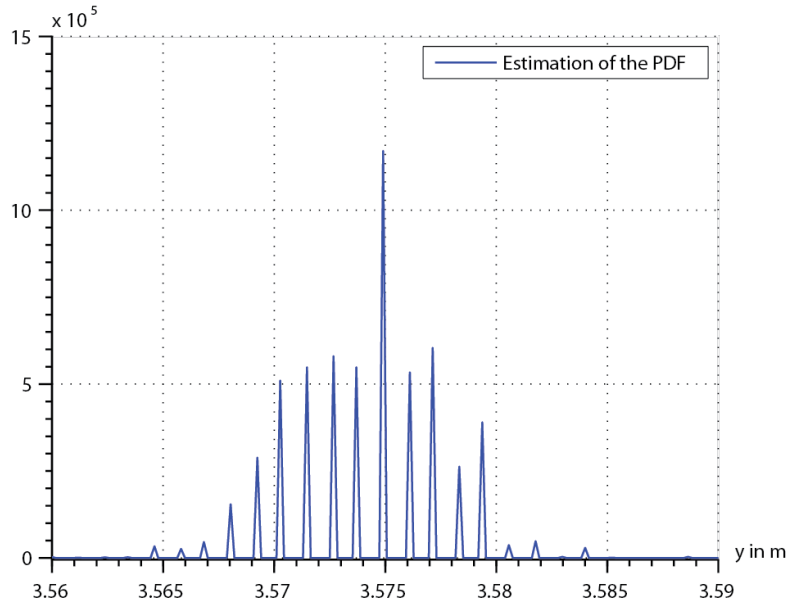

Figure 5.17: Estimation of the power density function of the rotor fixed at $y = 3.575\ mm$

Figure 5.17 shows the estimated power density function and indicates that the values are normally distributed. Of course one estimation does not proof, but estimations of the

PDF[5] at multiple displacement points were comparable in shape.

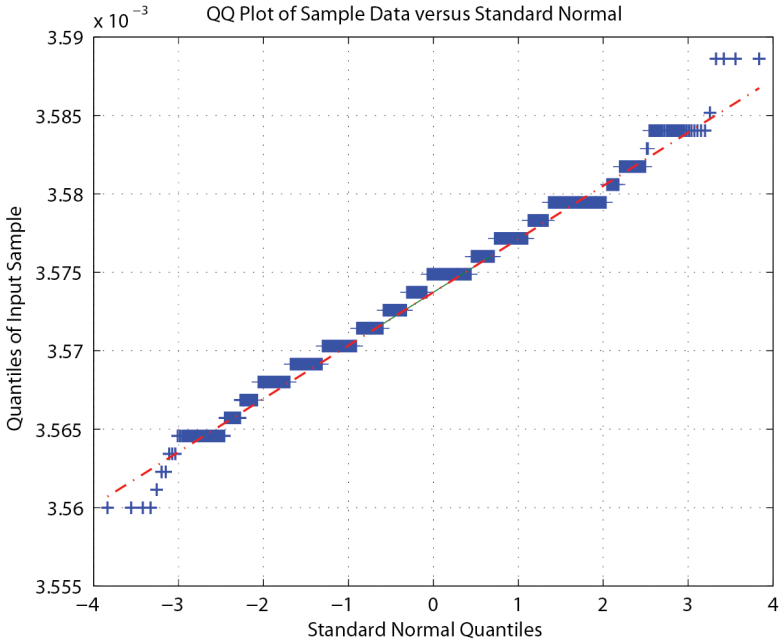

Figure 5.18: Corresponding QQ-plot of the measurement data of figure 5.17

Figure 5.18 confirms the assumption that the measurement noise is normally distributed. The QQ-plot compares the empiric sampled data with the theoretical model of the statistical distribution.

Another good function to go more into the statistical details of the measurement signals is the FFT represented in Figure 5.19. The fact that the noise floor of the measurement noise at 17 mm is approximately ten times (20 dB) higher than the noise floor at 1 mm can also be observed in Figure 5.16 where the standard deviation increases equally.

[5]Power density function

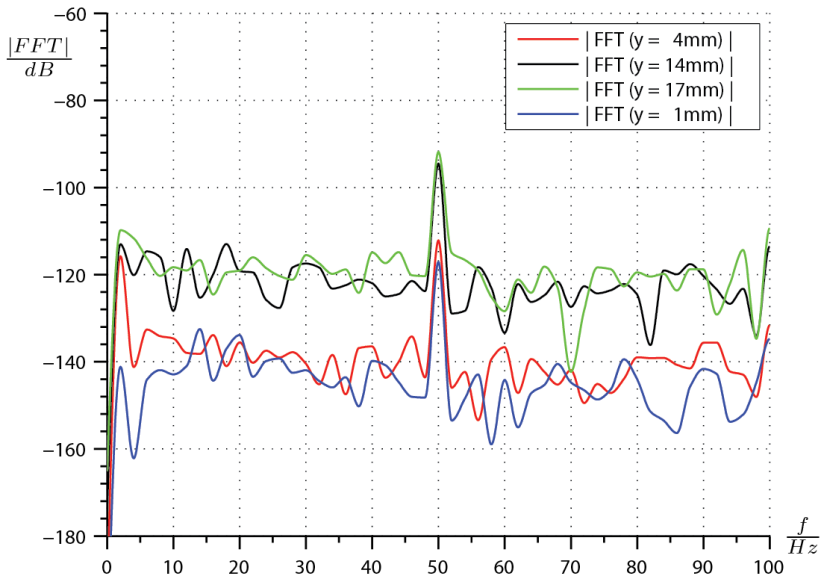

Figure 5.19: Absolute values of the fast Fourier transformation of several rotor positions

The peaks at 50 Hz are clearly induced by the main power supply, somewhere between the measurement board and dSpace control unit. After this discovery the main cables were reconfigured and the measurement signal was shielded.

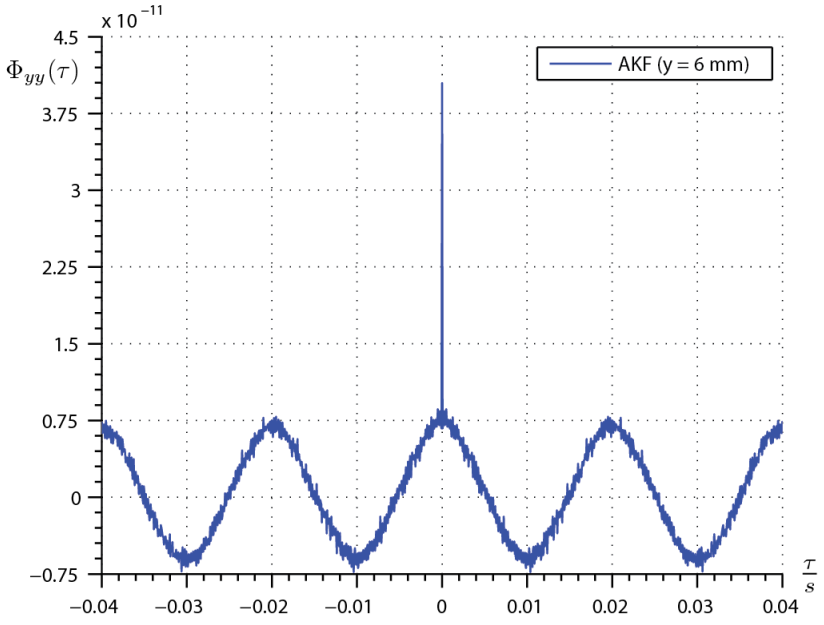

Figure 5.20: Auto correlation function of the position signal noise at y = 6 mm

The auto-correlation function (ACF) in figure 5.20 proves that there is a substantial amount of induced voltage from the main power supply in the measurement noise. The

percentage of 50 Hz noise is 18 percent of the whole noise power. This means that preventing remaining mains hum in the measurement signal could reduce the SNR[6] and the noise floor by $-7.4\ dB$ as shown in equation 5.6

$$10 \cdot log\left(\frac{18\ \%}{100\ \%}\right) = -7.4\ dB \tag{5.6}$$

The remaining 82 % of the signal noise power is white and therefore consists of thermal noise and amplification noise.

5.3.3 Dynamic Properties

To investigate the dynamic properties of the eddy current displacement measurement a linear motor was used to oscillate the rotor.

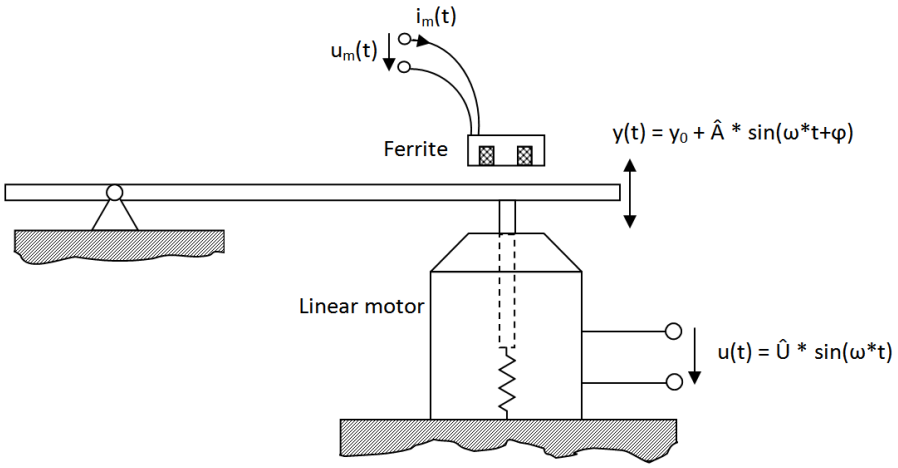

Figure 5.21: Configuration to research the dynamic properties

This setup is generally not optimal, because the displacement measurement should be monitored with another measurement system to verify the data. Figure 5.22 shows a curve that drops down with a slope of two decades per decade over frequency with a cut-off frequency of 25 Hz. This characteristic describes the electromechanic system of the linear shaker motor and the mass-spring system. The linear motor is a PT1 element with voltage $u(t)$ as input and position $y(t)$ as output. The mass-spring system is the second PT1 element. Generally, the frequency response in figure 5.22 is not a measurement of the eddy current measurement's bandwidth. Nevertheless the assumption can be made that the measurement system does not attenuate the position signal.

[6]Signal to noise ratio

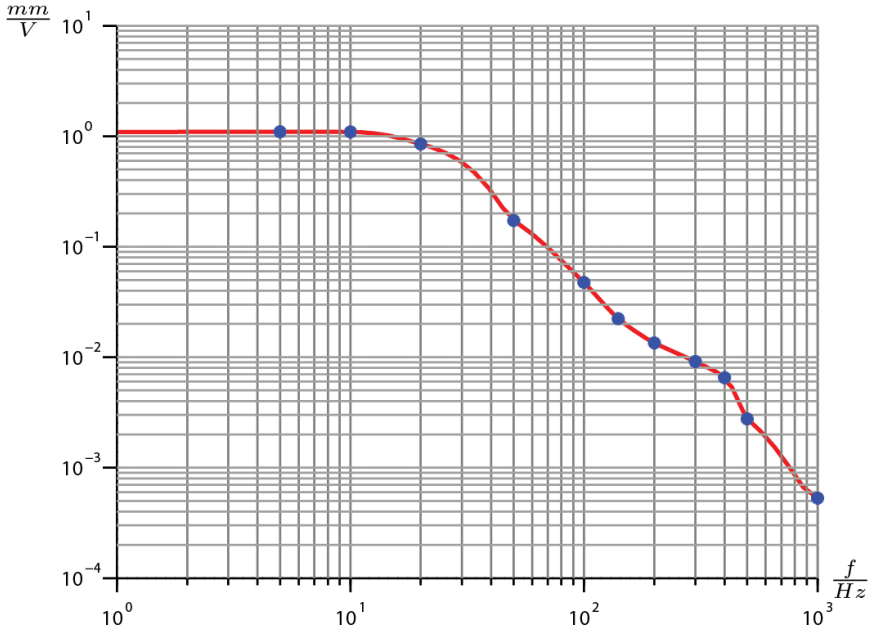

Figure 5.22: Logarithmic frequency response of the electromechanic rotor measured with the eddy current displacement measurement

Chapter 6

Control System

The whole control system, that consisting of the inputs and outputs and the central processing unit, is provided by a dSpace "Real Time Interface" system. The digital multi analog input board ds 2003 features 32 inputs. Two 16 channel multiplexing ADC units convert each channel with a 16 bit resolution within 5.6 micro seconds. The digital multi analog output board ds 2103 features 32 channels with a 14 bit resolution and 10 micro seconds settling time. The multitasking operating system is programmed with Matlab Simulink. For real time monitoring, measuring and manually controlling, the "dSpace control desk" software provides the necessary human machine interface. With this software any constant, variable or signal, can be displayed, saved, or manipulated in real time. This hardware is made for "rapid prototyping" which allows simple servicing and testing.

6.1 Current Controller

To establish attraction experiments with the electro magnet a current controller is a prerequisite to find acceptable values for the bias current i_R. This is done with the rotor blocked at the nominal displacement y_R. Beginning at the maximum current, a negative current slope decreases the attractive force until the rotor falls down. This experiment is repeated iteratively, approximating the bias current i_R. The lower the current slope, the more precisely is the obtained value i_R.

Since the term "current control" implies a current amplifier driven by a current signal, the correct classification for controlling the electro magnet's current with an amplified voltage signal is called "voltage control".

The current voltage relationship of the electro magnet is described in equation 6.1.

$$u = Ri + L\frac{d}{dt}i + k_u\frac{d}{dt}y \tag{6.1}$$

One basic controller design method is the frequency response analysis. For this approach the first two terms of eq. 6.1 lead to the frequency domain transfer function.

$$G_i(s) = \frac{i(s)}{u(s)} = \frac{1}{R + sL} \tag{6.2}$$

The next step is the determination of the parameters R and L. The resistance R is measured at room temperature $T = 21°$ with the "Keithley 2100 Digital Mulitmeter" using its four-wire connection. $R = 3.23\ \Omega$. The winding's voltage and current is measured online. This enables the possibility to estimate the winding's temperature in operation.

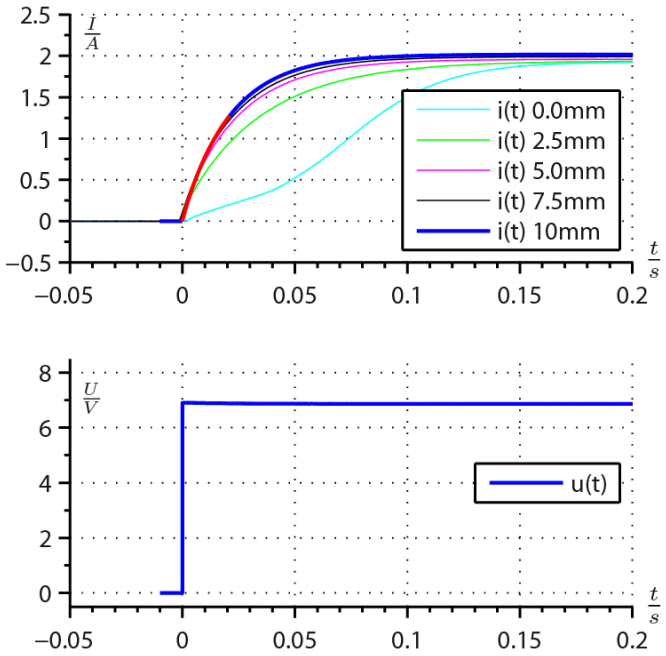

Figure 6.1: Rising current slopes at different rotor positions

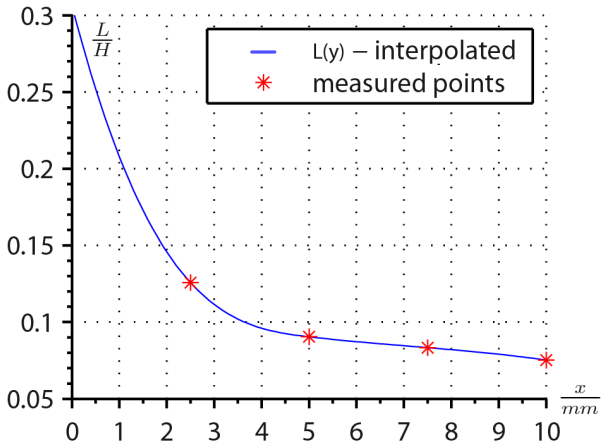

Figure 6.2: Inductance L as a function of the rotor displacement y

To measure the winding's inductance a voltage step is applied. The time constant of the rising current slope leads to the inductance $L = \tau \cdot R^{-1}$. The inductance L of the electro magnet, of course, is a function of the rotor's displacement y. Figure 6.1 shows current slopes at different rotor positions. The electro magnet's current curve in the position $y = 0\ mm$ starts with the lowest current slope caused by the "closed" iron loop that features the highest possible inductance. When the current reaches 0.5 A at $t = 0.05\ s$, the current slope increases due to the iron's non-linear properties. Figure 6.2 shows the variation of L as a function of the rotor displacement y.

6.1.1 Frequency Response Control Unit Design

The profit of this method is that with small effort, a suitable controller can be designed, which fulfills the desired specifications.

- No static control deviation $\lim_{t\to\infty} e(t) = 0\big|_{r(t)=\sigma(t)}$
- The desired rise time or control bandwidth specified by the cut-off angular frequency ω_c
- The desired overshoot specified by the phase margin Φ_R

$$\omega_R \cdot tr \approx 1.5 \tag{6.3}$$

$$\Phi_c + Mp \approx 70\ \% \tag{6.4}$$

A big disadvantage of this fast implementation is that this controller consists of constant values and cannot be adapted. Any changes of the plant in time due to aging or temperature changes have to be compensated by the controller. The first step is to transform the continuous time transfer function $G_i(s)$ of the plant into a discrete time transfer function.

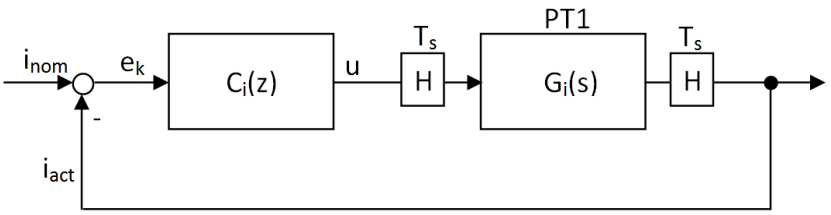

Figure 6.3: Control loop of the current controller with the corresponding plant

$$G_i(z) = z^{-1} \cdot \left(1 - z^{-1}\right) \cdot \mathscr{Z}\left\{\frac{G_i(s)}{s}\right\} \tag{6.5}$$

To design a controller with the *sisotool* Matlab function, the discrete time transfer function $G_i(z)$ needs to be transformed using the bilinear transformation. This is necessary to shape the controller's open loop frequency response without restrictions. Another reason to transform $G_i(z)$ into $G_i(q)$ is that the solution of the complex variable z (see eq. 6.6) is more difficult than the solution of the complex variable q (see eq. 6.7).

$$z = e^{j\omega \cdot T_s} = \frac{1 + j\Omega\frac{T_s}{2}}{1 - j\Omega\frac{T_s}{2}} \tag{6.6}$$

$$q = \sigma + j\Omega = \frac{2 \cdot j}{T_s} \cdot tan\left(\frac{\omega}{2}\right) \tag{6.7}$$

This leads to the q-transfer function $G_i(q)$.

$$G_i(q) = G_i(z)\Big|_{z=\frac{1+q\frac{T_s}{2}}{1-q\frac{T_s}{2}}} \tag{6.8}$$

After shaping the open loop frequency response, the q-transfer function of the controller $C_i(q)$ can be transformed inversely into $C_i(z)$ using equation 6.9.

$$C_i(z) = C_i(q)\Big|_{q=\frac{2}{T_s}\cdot\frac{z-1}{z+1}} \tag{6.9}$$

After this transformation, the open loop transfer function $L_i(z)$ and the closed loop transfer function $T_i(z)$ could be used to design a superior controller. The plant for the superior controller would be the closed loop transfer function of the subsidiary controller.

$$L_i(z) = C_i(z) \cdot G_i(z) \tag{6.10}$$

$$T_i(z) = \frac{L_i(z)}{1 + L_i(z)} \tag{6.11}$$

6.1.2 Simulation and Test of the Current Controllers

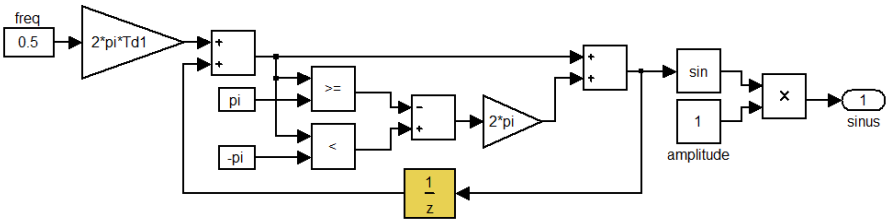

(a) Sinus test function generator

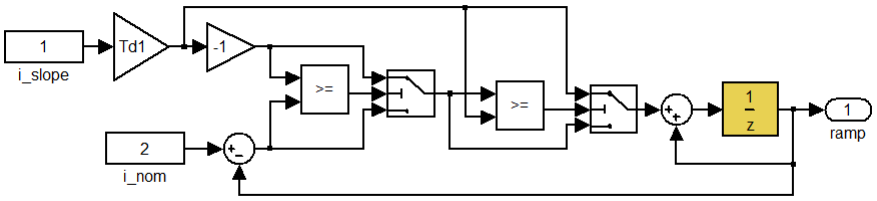

(b) Slope test function generator

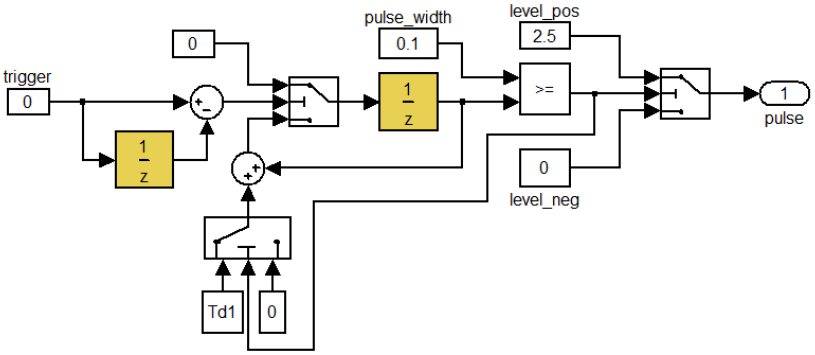

(c) Pulse test function generator

Figure 6.4: Adjustable functions for current controller testing

First the controller has to prove oneself in a simulation. An important detail is to take the ADCs and DACs sample-and-hold time and resolution into account. A current pulse is used to test the controller's step response. The simulation provides the possibility to adjust the necessary anti-windup loop safely. The anti-windup loop is inevitable because the current controller's control variable is limited to the amplifier's minimum and maximum output voltage.

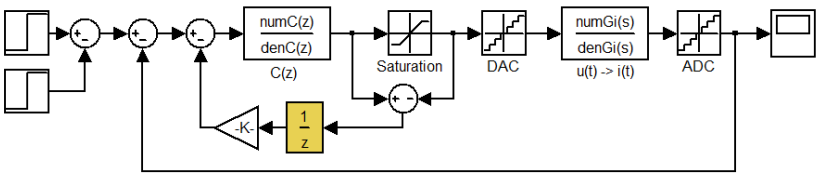

Figure 6.5: Step function test simulation of the current controller

The same applies to the PI Controller in Figure 6.6. The reason why the proportional and the integral part of the controller can be switched on and off separately, is to explore the different effects. Another advantage is that flipping between the PI controller and the frequency response analysis controller is possible. Therefore it is important to fully deactivate the integration and anti-windup loop and reset the integrator state. This is necessary to make sure, no remaining values could cause troubles. This enable-variable $enable_{INT}$ is also linked to the emergency shutdown.

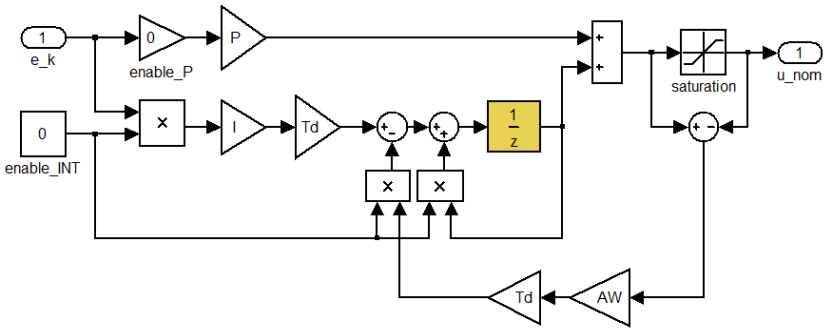

Figure 6.6: Selectable PI controller

The whole control structure can be seen in Figure 6.7.

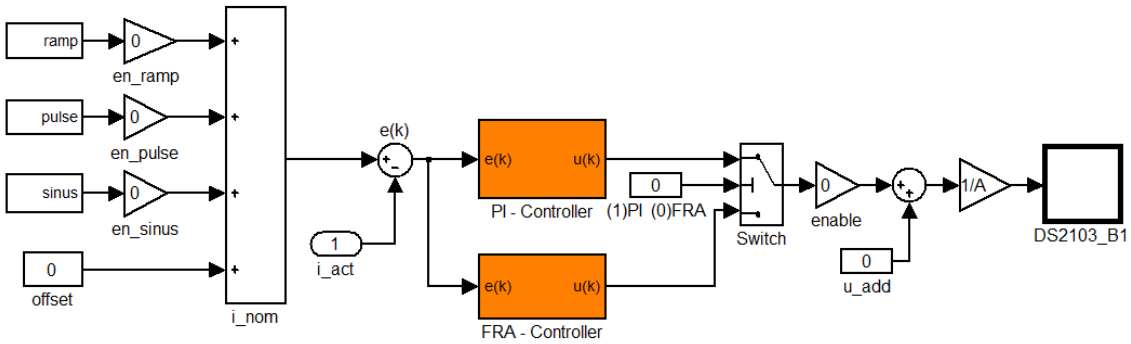

Figure 6.7: Current Control structure with selectable controller and several adjustable test functions

6.2 State Space Control Structure

The state space representation is well known and commonly used to control electromechanic systems. An advantage is that the derivation of the system's differential equations can be mathematically derived with Lagrange's Formalism. Control structures like state space controllers are easy to implement once the state space model and the state space controller has been proved in simulation. Another advantage is that non-measureable states can be estimated using an observer. Varying parameters like the coil's inductance and resistance can be taken into account and therefore improve the controller's performance. A disadvantage is the preliminary mathematical effort.

Every single magnetic bearing component like the axial bearing, horizontal radial bearing or vertical radial bearing can be represented by a SISO[1] state space model of the form:

$$\frac{\partial \underline{\mathbf{x}}}{\partial t} = \underline{\mathbf{A}} \cdot \underline{\mathbf{x}} + \underline{\mathbf{b}} \cdot u \tag{6.12}$$

$$y = \underline{\mathbf{c}}^T \cdot \underline{\mathbf{x}} + d \cdot u \tag{6.13}$$

6.2.1 Derivation of the non-linear partial differential equations

For a mechanical system the equations of motion can be derived by inserting the Lagrangian into the Euler-Lagrange Equation. The Lagrangian $\mathscr{L}$ describes the dynamics of the system, where $\mathscr{T}$ is kinetic energy and $\mathscr{V}$ is the potential energy.

$$\mathscr{L} = \mathscr{T} - \mathscr{V} \tag{6.14}$$

$$\frac{d}{dt}\left(\frac{\partial \mathscr{L}}{\partial \dot{q}_j}\right) - \frac{\partial \mathscr{L}}{\partial q_j} = 0 \tag{6.15}$$

The Euler-Lagrange equation of second kind is used to describe system where just conservative potential forces occur. The extended Euler Lagrange equation of second kind for non-conservative systems containing non-potential forces is described in equation 6.16 where $\mathscr{Q}$ is the generalized force and $\mathscr{P}$ is the dissipation function.

$$\frac{d}{dt}\left(\frac{\partial \mathscr{L}}{\partial \dot{q}_j}\right) - \frac{\partial \mathscr{L}}{\partial q_j} = -\frac{\partial \mathscr{P}}{\partial \dot{q}_j} + \mathscr{Q}_j \tag{6.16}$$

[1] Single input single output

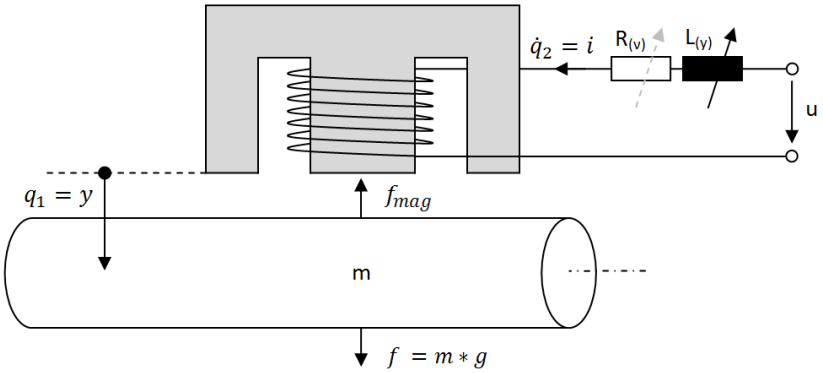

Figure 6.8: Electromechanic system with the generalized coordinates

Starting with the electromechanic system illustrated in Fig.6.8 the kinetic energy and the potential energy can be formulated as:

$$\mathscr{T} = \frac{m \cdot \dot{q}_1^2}{2} - \frac{L\,(q_1) \cdot \dot{q}_2{}^2}{2} \tag{6.17}$$

$$\mathscr{V} = m \cdot g \cdot -q_1 \tag{6.18}$$

Since the coordinate system is upside down, the potential energy is negative. Inserting $\mathscr{T}$ and $\mathscr{V}$ into the Lagrangian $\mathscr{L}$ in 6.14, $\mathscr{L}$ can be expressed as:

$$\mathscr{L} = \frac{m\dot{q}_1^2}{2} - \frac{L\,(q_1) \cdot \dot{q}_2{}^2}{2} + m \cdot g \cdot q_1 \tag{6.19}$$

To finally obtain the extended Euler-Lagrange equation of second kind, the dissipation function and the generalized force have to be defined.

$$\mathscr{P}_1 = 0, \qquad \mathscr{P}_2 = \frac{R(\nu) \cdot \dot{q}_2^2}{2} \tag{6.20}$$

$$\mathscr{Q}_1 = 0, \qquad \mathscr{Q}_2 = u \tag{6.21}$$

Here the dissipation function consists of ohmic losses. The only non-conservative force is the voltage source. To keep the overview, all derivatives are listed below before inserting into equation 6.16.

$$\frac{\partial \mathscr{L}}{\partial q_1} = m \cdot g - \frac{1}{2} \cdot \frac{L\,(q_1) \cdot \dot{q}_2^2}{\partial q_1} \tag{6.22}$$

$$\frac{d}{dt}\left(\frac{\partial \mathscr{L}}{\partial \dot{q}_1}\right) = m \cdot \ddot{q}_1 \tag{6.23}$$

$$\frac{\partial \mathscr{L}}{\partial q_2} = 0 \tag{6.24}$$

$$\frac{d}{dt}\left(\frac{\partial \mathscr{L}}{\partial \dot{q}_2}\right) = L\left(q_1\right) \cdot \ddot{q}_2 - \frac{L\left(q_1\right)}{\partial q_1} \cdot \dot{q}_1 \cdot \dot{q}_2 \tag{6.25}$$

$$-\frac{\partial \mathscr{P}_2}{\partial \dot{q}_2} = R(\nu) \cdot \dot{q}_2 \tag{6.26}$$

Inserting equations 6.22 to 6.26 into 6.16, results in 2 partial differential equations.

$$m\ddot{q}_1 - m \cdot g + \frac{1}{2} \cdot \frac{L\left(q_1\right) \cdot \dot{q}_2^2}{\partial q_1} = 0 \tag{6.27}$$

$$L\left(q_1\right) \cdot \ddot{q}_2 - \frac{L\left(q_1\right)}{\partial q_1} \cdot \dot{q}_1 \cdot \dot{q}_2 = -R(\nu) \cdot \dot{q}_2 + u \tag{6.28}$$

With $q_1 = y$ and $\dot{q}_2 = i$ equations 6.27 and 6.28 can be converted to:

$$\ddot{y} = g - \frac{\partial L\left(y\right)}{\partial y} \cdot \frac{i^2}{2 \cdot m} \tag{6.29}$$

$$\dot{i} = -\frac{R(\nu)}{L\left(y\right)} \cdot i + \frac{\partial L\left(y\right)}{\partial y} \cdot \frac{\dot{y} \cdot i}{L\left(y\right)} + \frac{u}{L\left(y\right)} \tag{6.30}$$

The Inductance $L\left(y\right)$ is a non-linear function as seen in Fig. 6.2. Since the non-linear system has to be linearized in the operating point to set up a linear state-space controller, the inductance L can also be linearized in the operating point y_R:

$$L\left(y\right) = L_0 + \frac{\Delta L \cdot y_R}{y} \tag{6.31}$$

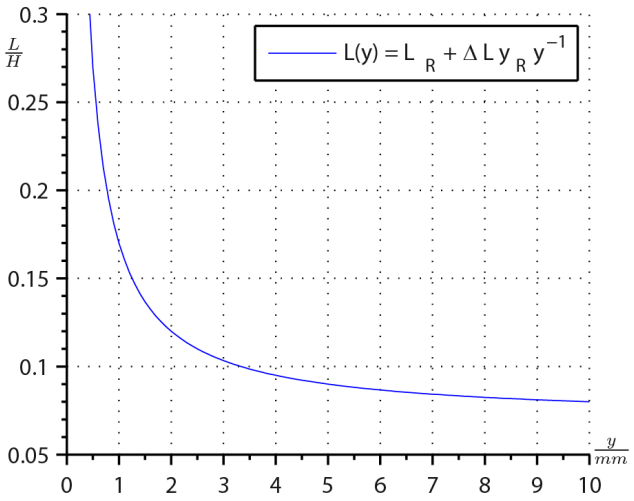

Figure 6.9: Approximation of L(y)

The inductance $L(y)$ is approximated with the inductance L_0 and the inductance slope ΔL [13]. The function $L(y)$ shown in Fig. 6.9 is very similar to the measured inductance $L(x)$ in Fig. 6.2. For values of y close to zero the approximation approaches infinity. This is not critical because the valid rotor displacement at $y_R = 5\ mm$ is $\pm 4\ mm$. Additionally, the inductance $L(y)$ in the non-linear system will be saturated with the maximum inductance $L_{max} = 0.3\ H$.

$$\frac{\partial L(y)}{\partial y} = \frac{\Delta L \cdot y_R}{y^2} \tag{6.32}$$

With the approximated inductance inserted, the equations 6.29 and 6.30 result in:

$$\ddot{y} = g - \frac{\Delta L \cdot y_R}{y^2} \cdot \frac{i^2}{2 \cdot m} \tag{6.33}$$

$$\dot{i} = -\frac{R(\nu)}{L(y)} \cdot i + \frac{\Delta L \cdot y_R}{y^2} \cdot \frac{\dot{y} \cdot i}{L(y)} + \frac{u}{L(y)} \tag{6.34}$$

With the equations (6.33) and (6.34) and the three state variables $y = x_1$, $\dot{y} = x_2$ and $i = x_3$ the non-linear system can be summarized:

$$\dot{x}_1 = x_2 \tag{6.35a}$$

$$\dot{x}_2 = g - \frac{\Delta L \cdot y_R}{x_1^2} \cdot \frac{x_3^2}{2 \cdot m} \tag{6.35b}$$

$$\dot{x}_3 = -\frac{R(\nu)}{L(x_1)} \cdot x_3 + \frac{\Delta L \cdot y_R}{x_1^2} \cdot \frac{x_2 \cdot x_3}{L(x_1)} + \frac{u}{L(x_1)} \tag{6.35c}$$

This non-linear system is used to test linear controllers and observers, derived from the linearized model of subsection 6.2.2

$$\underbrace{\begin{bmatrix}\dot{x}_1\\ \dot{x}_2\\ \dot{x}_3\end{bmatrix}}_{\underline{\dot{x}}} = \underbrace{\begin{bmatrix}p_1\left(\underline{x},u\right)\\ p_2\left(\underline{x},u\right)\\ p_3\left(\underline{x},u\right)\end{bmatrix}}_{\underline{p}(\underline{x},u)} \tag{6.36}$$

6.2.2 Linearized State Space Model

The linearized system in the operating point $\underline{x}_R$ is obtained from the derivative of the non-linear system in the operating point with respect of the state variables.

The system matrix $\underline{A}$ is derived by:

$$\underline{A} = \left.\frac{\partial \underline{p}(\underline{x},u)}{\partial \underline{x}}\right|_{(\underline{x}=\underline{x}_R,u=u_R)} \tag{6.37}$$

The input vector $\underline{b}$ is derived by:

$$\underline{b} = \left.\frac{\partial \underline{p}(\underline{x},u)}{\partial u}\right|_{(\underline{x}=\underline{x}_R,u=u_R)} \tag{6.38}$$

To formulate the linearized system, the state variable vector $\underline{x}$ and the input signal u have to be substituted with:

$$\underbrace{\begin{bmatrix}x_1\\ x_2\\ x_3\end{bmatrix}}_{\underline{x}} = \underbrace{\begin{bmatrix}x_{1R}\\ x_{2R}\\ x_{3R}\end{bmatrix}}_{\underline{x}_R} + \underbrace{\begin{bmatrix}\Delta x_1\\ \Delta x_2\\ \Delta x_3\end{bmatrix}}_{\Delta\underline{x}} \tag{6.39}$$

$$u = u_R + \Delta u \tag{6.40}$$

$$y = y_R + \Delta y \tag{6.41}$$

The operating point $\underline{\dot{x}} = \underline{0} = \underline{p}(\underline{x},u)\Big|_{\underline{x}=\underline{x}_R,u=u_R}$ with $x_{1R} = y_R$ leads to:

$$x_{2R} = 0 \tag{6.42}$$

$$x_{3R} = \sqrt{\frac{2\cdot m\cdot g\cdot y_R}{\Delta L}} \tag{6.43}$$

$$L_R = L(y_R) = L_0 + \Delta L \tag{6.44}$$

Now the linearized system can be written as:

$$\underbrace{\begin{bmatrix}\Delta\dot{x}_1\\ \Delta\dot{x}_2\\ \Delta\dot{x}_3\end{bmatrix}}_{\Delta\underline{\dot{x}}} = \underbrace{\begin{bmatrix}0 & 1 & 0\\ \frac{2g}{y_R} & 0 & -\sqrt{\frac{2g\cdot\Delta L}{m\cdot y_R}}\\ 0 & \sqrt{\frac{2mg\cdot\Delta L}{y_R\cdot L_R^2}} & -\frac{R}{L_R}\end{bmatrix}}_{\underline{A}} \cdot \underbrace{\begin{bmatrix}\Delta x_1\\ \Delta x_2\\ \Delta x_3\end{bmatrix}}_{\Delta\underline{x}} + \underbrace{\begin{bmatrix}0\\ 0\\ \frac{1}{L_R}\end{bmatrix}}_{\underline{b}} \cdot \Delta u \tag{6.45}$$

$$\Delta y = \underbrace{\begin{bmatrix}1 & 0 & 0\end{bmatrix}}_{\underline{c}^T} \cdot \underbrace{\begin{bmatrix}\Delta x_1\\ \Delta x_2\\ \Delta x_3\end{bmatrix}}_{\Delta\underline{x}} \tag{6.46}$$

6.2.3 Discrete Time State Space Model

With the discrete sampling time T_d the linear and discrete time state space model can be described by:

$$\Delta\underline{x}_{k+1} = \underline{A}_d \cdot \Delta\underline{x}_k + \underline{b}_d \cdot \Delta u_k \tag{6.47}$$

$$\Delta y_k = \underline{c}_d^T \cdot \Delta\underline{x}_k \tag{6.48}$$

$$\underline{A}_d = e^{\underline{A}\cdot T_d} \tag{6.49}$$

$$\underline{b}_d = \int_0^{T_d} e^{\underline{A}\cdot\tau} \cdot \underline{b} \cdot d\tau \tag{6.50}$$

$$\underline{c}_d = \underline{c} \tag{6.51}$$

The discrete state space model's eigenvalues can be predefined with the state space controller. To find a suitable eigenvalue combination the state space controller is simulated in Matlab Simulink with the non-linear state space model as simulation plant.

The optimal eigenvalues of the new system matrix $(\underline{A}_d - \underline{b}_d \cdot \underline{h}^T)$ are chosen experimentally. Due to stability the eigenvalues of the system matrix have to be inside the unit circle. With the control signal r_k the new discrete system with the feedback controller is

described by:

$$\Delta \underline{x}_{k+1} = \underbrace{(\underline{A}_d - \underline{b}_d \cdot \underline{h}^T)}_{\underline{\Phi}} \cdot \Delta \underline{x}_k + \underline{b}_d \cdot r_k \tag{6.52}$$

$$\Delta y_k = \underline{c}_d^T \cdot \Delta \underline{x}_k \tag{6.53}$$

To implement the state space controller with its control law $\Delta u_k = -\underline{h}^T \cdot \Delta \underline{x}_k$, the whole state vector $\Delta \underline{x}$ has to be determined. The states $\Delta x_1 = \Delta y$ and $\Delta x_3 = \Delta i$ are measured directly. The state $\Delta x_2 = \dot{y}$ which is not measured can either be differentiated from Δx_1 or can be estimated using an observer.

6.2.4 Simulation of the state space controller

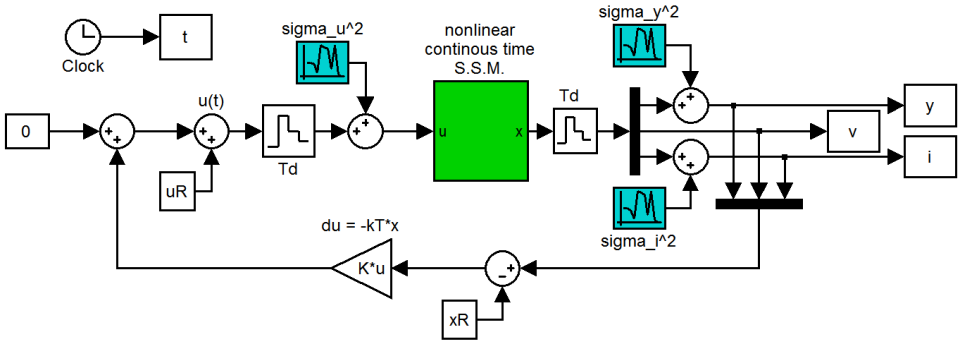

Figure 6.10: Simulation of the state space controller

The DAC[2]'s quantization noise is simulated as additional random white noise with variance σ_u^2. The standard deviation σ_u of the $n = 16$ bit DAC and the voltage range of the amplifier of $\pm 20V$ is calculated by:

$$\sigma_u = \frac{(U_{max} - U_{min})}{2^n \cdot \sqrt{12}} = 1.76\ mV \tag{6.54}$$

The position signal's standard deviation σ_y is chosen from tabular 5.1 in section 5.3. The standard deviation of $y = 5\ mm$ is calculated by linear interpolation.

$$\sigma_y = \sigma_y\big|_{y=y_R} = 5.14\ \mu m \tag{6.55}$$

[2]Digital to analog converter

The theoretical minimum current signal's variance due to the ADC conversion can be derived. Since the current signal is provided by the amplifier's internal current sensor, the standard deviation σ_i has to be measured. Eq. 6.57 shows the measured value for the current signal's standard deviation.

$$\sigma_{i,min} = \frac{(I_{max} - I_{min})}{2^n \cdot \sqrt{12}} = \frac{(5 - (-5))}{2^{16} \cdot \sqrt{12}} = 44.05\ \mu A \tag{6.56}$$

$$\sigma_i = 673.4\ \mu A \tag{6.57}$$

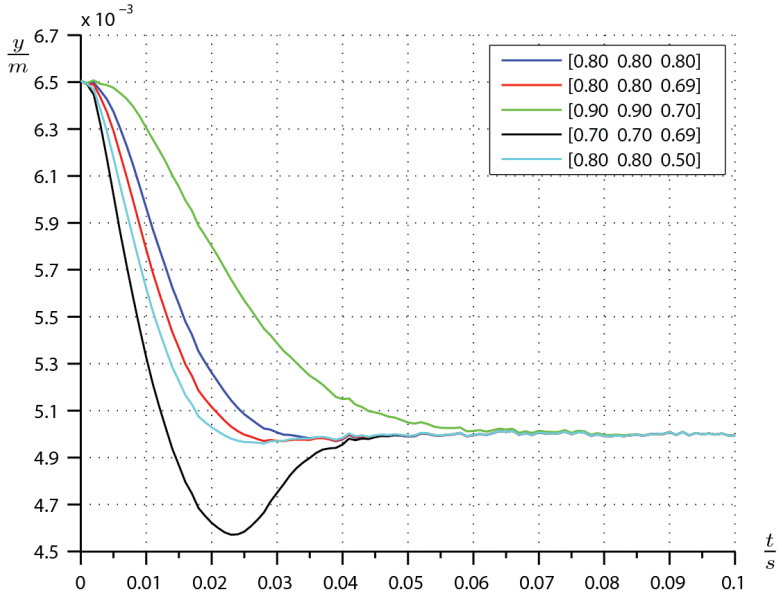

Figure 6.11: Simulation results of the state space controller with different eigenvalue configurations

Figure 6.11 shows the results of four different simulation runs. An important fact is that the state Δx_2 which is not available in the real control scheme was taken from the non-linear SSM[3] to find the optimal eigenvalues of the new system matrix $\hat{\underline{\Phi}}$. The simulation showed that a configuration of $eig(\hat{\underline{\Phi}}) = [0.8\ 0.8\ 0.5]$ is a good setting.

6.2.5 Estimating the rotor's velocity

There are different options to get a signal that represents the rotor's velocity:

[3]State Space Model

- A derivative of the rotor's position signal with a DT1[4] element
- An estimation of the velocity using a reduced observer
- An estimation of the velocity using a Kalman filter

Figure 6.12 shows three possible methods to derive the velocity $v = \frac{\partial y}{\partial t}$. The real velocity v is compared to the derivative of the position y in time. The rotor is deviated by 2 mm in position at the beginning of the simulation to get this velocity peak.

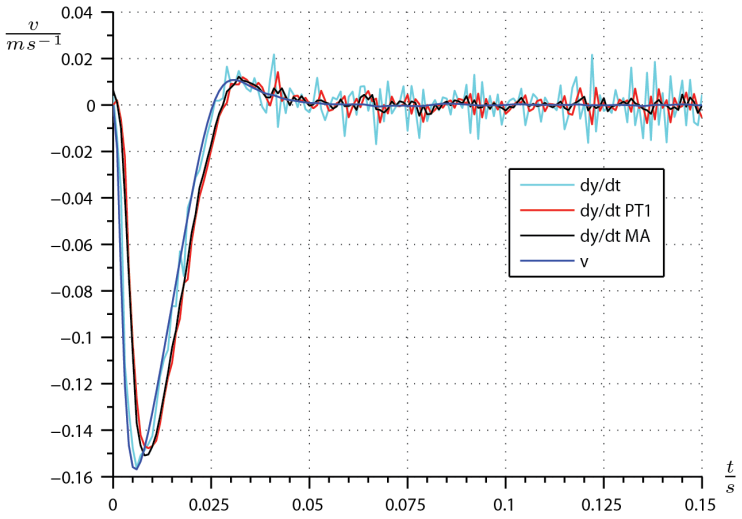

Figure 6.12: Comparison of the real velocity and the derived velocity

A brief comparison of the standard deviation of the different derived velocities:

- $\sigma_v = 0.2 \cdot 10^{-3}\ \frac{m}{s}$
- $\sigma_{\dot{y}} = 7.3 \cdot 10^{-3}\ \frac{m}{s}$
- $\sigma_{\dot{y}\ PT1} = 3.2 \cdot 10^{-3}\ \frac{m}{s}$
- $\sigma_{\dot{y}\ MA} = 1.9 \cdot 10^{-3}\ \frac{m}{s}$

The consequence of deriving the velocity is a tremendous increase of the standard deviation of the velocity signal. This leads to unnecessary voltage noise at the electro magnet which can be seen in figure 6.13. To reduce this noise the eigenvalues of the new system matrix $\underline{\hat{\Phi}}$ could be changed to slow down the controller.

[4]First order derivative element

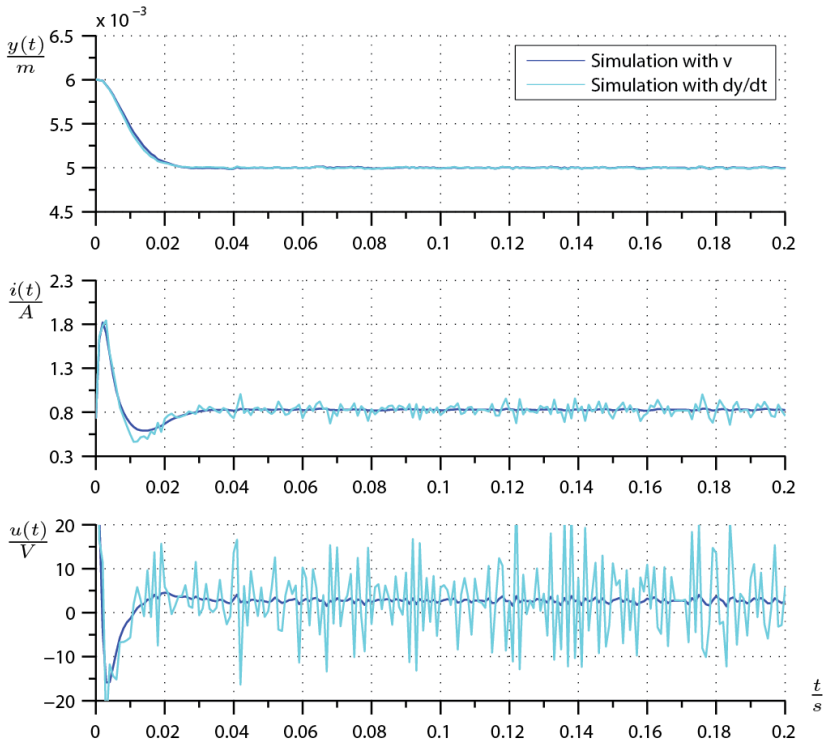

Figure 6.13: Consequence of deriving the velocity in simulation

The second option, estimating the velocity with a reduced observer is more elegant than the first option. Since the two states Δx_1 and Δx_3 are measured, the second system state Δx_2 can be estimated using the second differential equation from 6.45. To describe the reduced observer's equation 6.45 is enhanced by the correction term. [14]

$$\Delta\dot{\hat{x}}_2 = \frac{2g}{y_R} \cdot \Delta x_1 + \sqrt{\frac{2g \cdot \Delta L}{m \cdot y_R}} \cdot \Delta x_3 + f(2) \cdot \underbrace{(\Delta\hat{x}_2 - \Delta x_2)}_{e(t)} \tag{6.58}$$

The correction term is the estimation error weighted with the second eigenvalue $l(2) = [0\ 1\ 0]^T \cdot \underline{l}$ of the observer's system matrix $(\underline{\hat{\Phi}} - \underline{f} \cdot \underline{c}^T)$. The eigenvalues are specified for the transposed system, where the observer's system matrix is $(\underline{\hat{\Phi}}^T - \underline{c} \cdot \underline{f}^T)$.

An essential prerequisite is that the estimation error e_k shall diverge asymptotically, as defined in equation 6.59. This requires that the eigenvalues of the estimator system matrix $\underline{\widetilde{\Phi}} = (\underline{\hat{\Phi}} - \underline{f} \cdot \underline{c}^T)$ have a negative real part. Another prerequisite is that the system is absolute observable.

$$\lim_{t \to \infty} \|e(t)\| = \|\Delta x_2 - \Delta\hat{x}_2\| = 0 \tag{6.59}$$

Furthermore, continuing with equation 6.58 the discrete time observer equation can be written down as:

$$\Delta\dot{\hat{x}}_{2,k} = \frac{2g}{y_R} \cdot \Delta x_{1,k} + \sqrt{\frac{2g \cdot \Delta L}{m \cdot y_R}} \cdot \Delta x_{3,k} + f(2) \cdot \underbrace{(\Delta\hat{x}_{2,k} - \Delta x_{2,k})}_{e_k} \tag{6.60}$$

$$\lim_{k\to\infty} \|e_k\| = \|\Delta x_{2,k} - \Delta\hat{x}_{2,k}\| = 0 \tag{6.61}$$

To evaluate the quality of the reduced observer the estimated velocity is compared to the actual velocity in simulation.

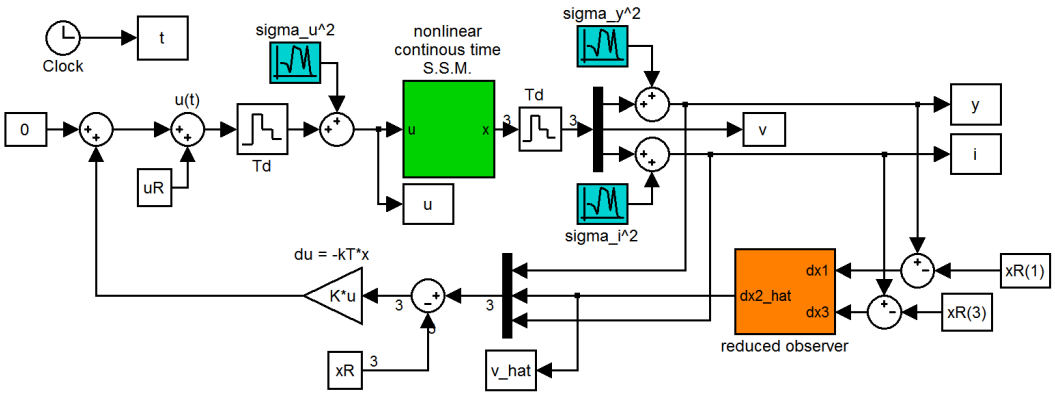

Figure 6.14: State feedback control loop with the reduced observer

After that the configured observer is tested in a simulation with the estimated state $\Delta\hat{x}_{2,k}$ fed back to the state controller. In figure 6.15 two different starting positions are simulated. The velocity is not estimated perfectly in high dynamic situations, although the state controller's performance is excellent and there is no unnecessary voltage noise as shown in figure 6.16.

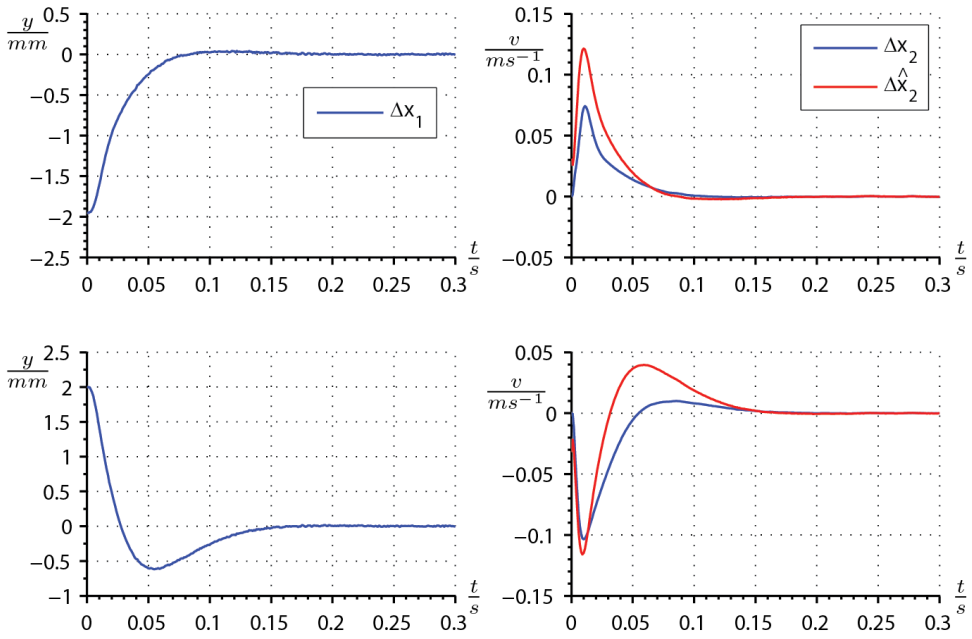

Figure 6.15: Two different extreme starting positions simulated with the reduced observer in the state feedback

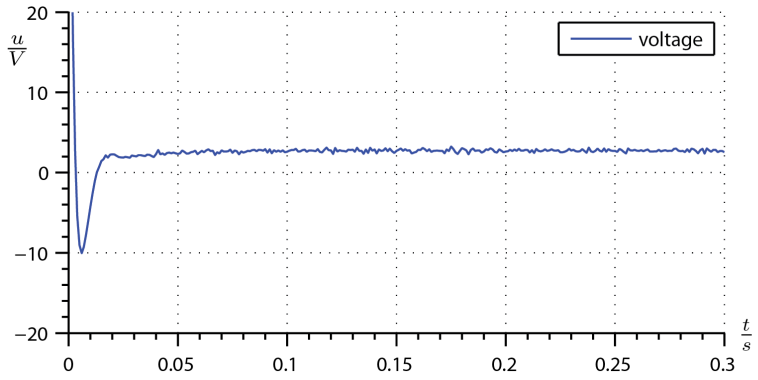

Figure 6.16: Voltage fed to the electro magnet from simulation in figure 6.15

The third option is to estimate the velocity using a Kalman filter [8] [7]. The following equations describe the discrete time state space model with the input noise w_k and the measurement noise v_k.

$$\Delta \underline{x}_{k+1} = \underline{A}_d \cdot \Delta \underline{x}_k + \underline{b}_d \cdot \Delta u_k + w_k \tag{6.62}$$

$$\Delta y_k = \underline{c}_d^T \cdot \Delta \underline{x}_k + v_k \tag{6.63}$$

The measurement noise v_k and the input noise w_k are uncorrelated, which is expressed in eq.6.64

$$\mathrm{E}\left\{v_k \cdot w_j\right\} = 0 \ , \quad \forall \ k, \ j \tag{6.64}$$

And both v_k and w_k are zero-mean.

$$\mathrm{E}\left\{v_k\right\} = 0 \ , \quad \forall \ k \tag{6.65}$$

$$\mathrm{E}\left\{w_k\right\} = 0 \ , \quad \forall \ k \tag{6.66}$$

To define the covariance matrix of the measurement noise $\underline{R}$ and the covariance matrix of the input noise $\underline{Q}$, the measurement noise v_k and the input noise w_k can be written in vector format.

$$\underline{v}_k = \begin{bmatrix} v_k \\ v_{k-1} \\ \vdots \\ v_0 \end{bmatrix}, \qquad \underline{w}_k = \begin{bmatrix} w_k \\ w_{k-1} \\ \vdots \\ w_0 \end{bmatrix} \tag{6.67}$$

$$\mathrm{E}\left\{\underline{w}_k \cdot \underline{w}_j^T\right\} = \begin{Bmatrix} \underline{Q} & \forall \ k = j \\ \underline{0} & \forall \ k \neq j \end{Bmatrix} \tag{6.68}$$

$$\mathrm{E}\left\{\underline{v}_k \cdot \underline{v}_j^T\right\} = \begin{Bmatrix} \underline{R} & \forall \ k = j \\ \underline{0} & \forall \ k \neq j \end{Bmatrix} \tag{6.69}$$

Continuing with the idea of a classical asymptotic observer, the original system from equation 6.63 is reproduced.

$$\Delta\underline{\hat{x}}_k = \underline{A}_d \cdot \Delta\underline{\hat{x}}_{k-1} + \underline{b}_d \cdot \Delta u_{k-1} + w_{k-1} \tag{6.70}$$

This leads to the "a-priori estimate value" $\Delta\underline{x}_k^*$

$$\Delta\underline{x}_k^* = A_d \cdot \Delta\underline{\hat{x}}_{k-1} + \underline{b}_d \cdot \Delta u_{k-1} \qquad \text{(I)} \tag{6.71}$$

Equation 6.71 is number (I) of the five Kalman equations. Further $\underline{P}_k^*$ is the covariance matrix of the predicated estimation error $\Delta\underline{x}_k^* - \Delta\underline{x}_k$

$$\underline{P}_k^* = \mathrm{E}\left\{\left(\Delta\underline{x}_k^* - \Delta\underline{x}_k\right) \cdot \left(\Delta\underline{x}_k^* - \Delta\underline{x}_k\right)^T\right\} \tag{6.72}$$

Without proof the second Kalman equation is defined by 6.73 and can be derived from eq. 6.72 [8] [7].

$$\underline{P}_k^* = \underline{A}_d \cdot \widetilde{\underline{P}}_{k-1} \cdot \underline{A}_d^T + \underline{Q} \qquad \text{(II)} \tag{6.73}$$

With the covariance matrix of the predicated estimation error, the Kalman vector $\underline{K}_k$ can be calculated with the third Kalman equation.

$$\underline{K}_k = \underline{P}_k^* \cdot \underline{c}_d \cdot \left(\underline{c}_d^T \cdot \underline{P}_k^* \cdot \underline{c}_d + \underline{R}\right)^{-1} \qquad \text{(III)} \tag{6.74}$$

This leads directly to the fourth Kalman equation which defines the "a-posteriori estimation value".

$$\Delta\underline{\hat{x}}_k = \Delta\underline{x}_k^* + \underline{K}_k \cdot \left(\Delta y_k - \underline{c}_d^T \cdot \Delta\underline{x}_k^*\right) \qquad \text{(IV)} \tag{6.75}$$

Finally Kalman equation number five describes the update of the error covariance matrix $\underline{\tilde{P}}_k$.

$$\widetilde{\underline{P}}_k = \left(\underline{I} - \underline{K}_k \cdot \underline{c}_d^T\right) \cdot \underline{P}_k^* \qquad \text{(V)} \tag{6.76}$$

Before the recursion starts, the initial error covariance matrix and the initial "a-priori estimated value", which is the initial state of the delay element in Figure 6.19, is defined.

$$\underline{P}_0^* = \mathrm{E}\left\{\left(\Delta\underline{x}_0^* - \Delta\underline{x}_0\right) \cdot \left(\Delta\underline{x}_0^* - \Delta\underline{x}_0\right)^T\right\} \tag{6.77}$$

$$\underline{P}_0^* = \begin{bmatrix} \left(\frac{0.0025}{2}\right)^2 & 0 & 0 \\ 0 & 1 \cdot 10^{-6} & 0 \\ 0 & 0 & 0.2 \end{bmatrix} \tag{6.78}$$

This means that at the beginning of the simulation, the difference between the real state space vector $\Delta\underline{x}_0$ of the linearized system and the predicated state space vector $\underline{x}_0^*$ of the linearized system is 2.5 mm in position, and an infinitesimal value in velocity and zero point two Ampere in current.

$$\underline{x}_0^* = \begin{bmatrix} 0 \\ 0 \\ 0 \end{bmatrix} \tag{6.79}$$

An important fact is that the Kalman equations (II), (III) and (V) can be computed independently before the simulation starts. Hence in simulation, the Kalman filter is only consisting of the two Kalman equations (I) and (IV).

With the idea of a classical observer containing the copy of the original system - Kalman equation (I) - and the correction term, the implementation for simulation is described by equation 6.80.

$$\Delta\underline{x}^*_{k+1} = \underbrace{\underline{A}_d \cdot \Delta\underline{x}^*_k + \underline{b}_d \cdot \Delta u_k}_{\text{copy}} + \underbrace{\hat{\underline{h}} \cdot (\Delta y_k - \underline{c}_d \cdot \Delta\underline{x}^*_k)}_{\text{correction if } \Delta y_k \neq \Delta y_k} \tag{6.80}$$

Assuming $\hat{\underline{h}} = \underline{A}_d \cdot \underline{K}_\infty$ with $\underline{K}_\infty = \lim_{k\to\infty} \underline{K}_k$

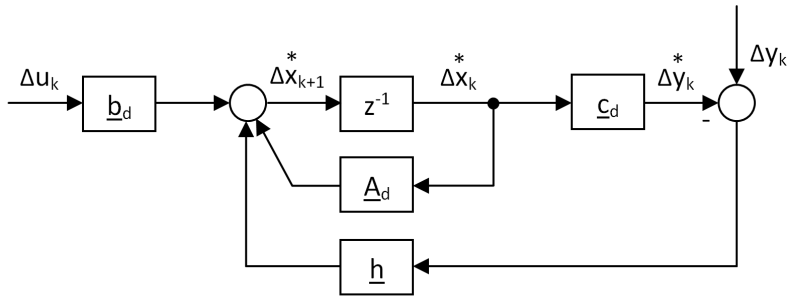

Figure 6.17: Signal flowchart of equation 6.80

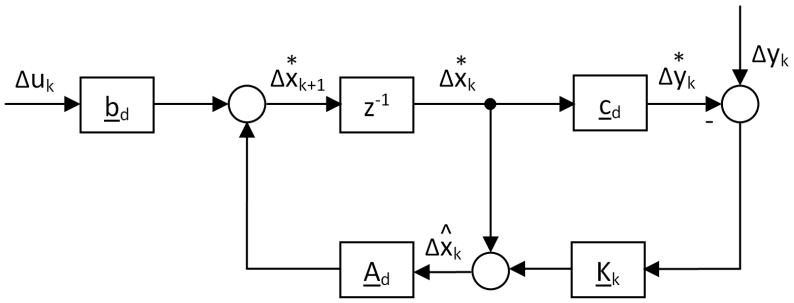

Figure 6.18: Adapted signal flowchart with implemented Kalman equation (IV)

Figure 6.18 contains all five Kalman equations [1]. The first and the fourth equation describe the flowchart and the other equations describe the calculation of $\underline{K}_k$. Since $\underline{K}_k$ is variant in time, it has to be calculated for each time step. This means with a sampling time of $Td = 1$ ms, $\underline{K}_k$ has to be calculated with the Kalman equations (II), (III) and (IV) 1000 times. This is quite a lot of overhead.

The variable $\underline{M}$ in figure 6.19 is $\underline{K}_\infty$ and was calculated using the Matlab-function "kalmd" and hardly differs from $\underline{K}_{1000}$.

$$\underline{K}_{1000} = \begin{bmatrix} 0.11046 \\ 6.46547 \\ 2.43438 \end{bmatrix}, \quad \underline{M} = \begin{bmatrix} 0.11046 \\ 6.46544 \\ 2.43438 \end{bmatrix} \tag{6.81}$$

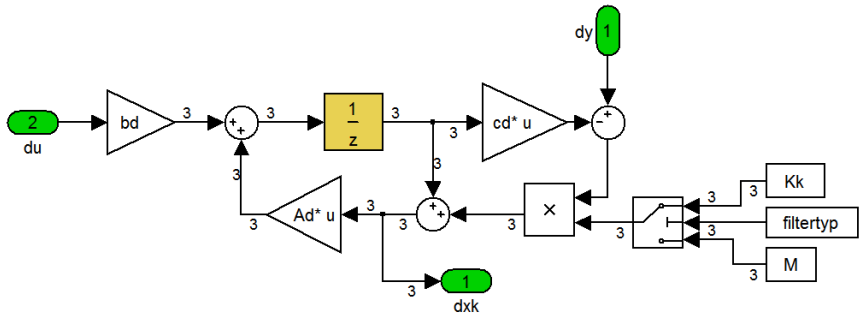

Figure 6.19: Simulink block diagram of the switchable optimal and suboptimal Kalman filter

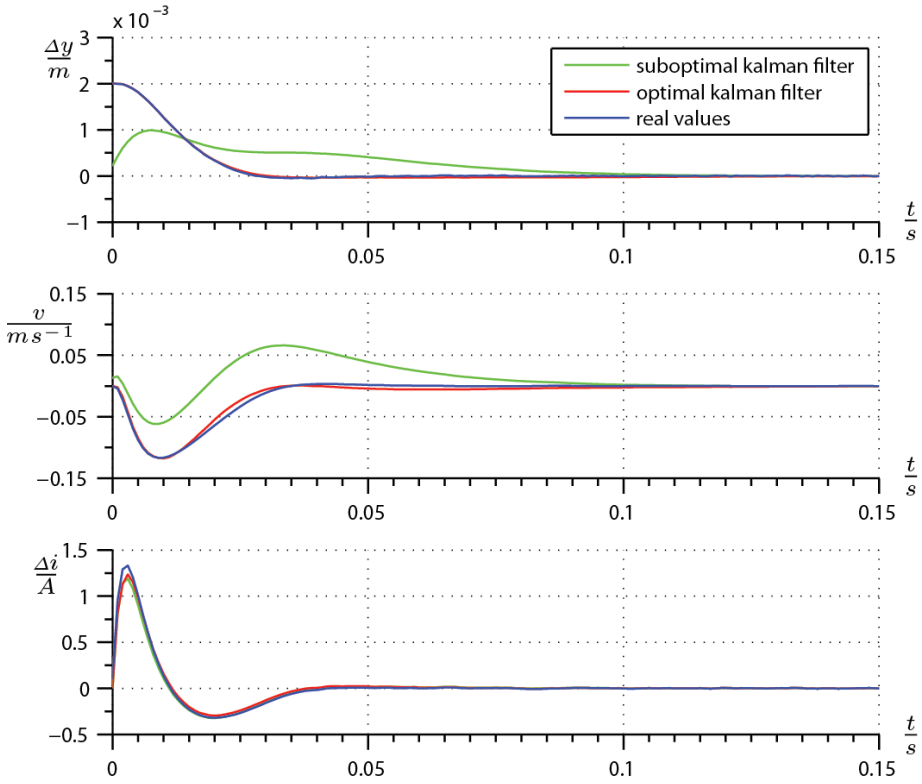

Figure 6.20: Suboptimal and optimal Kalman filter compared to real simulation values

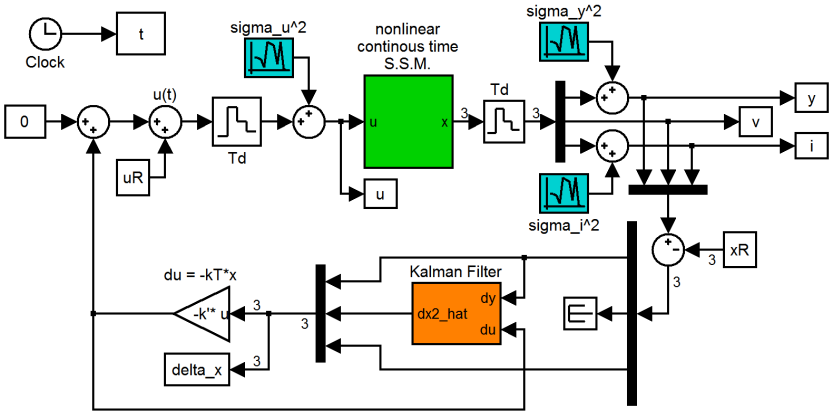

Figure 6.21: Recursion of the estimated velocity with the suboptimal and optimal Kalman filter

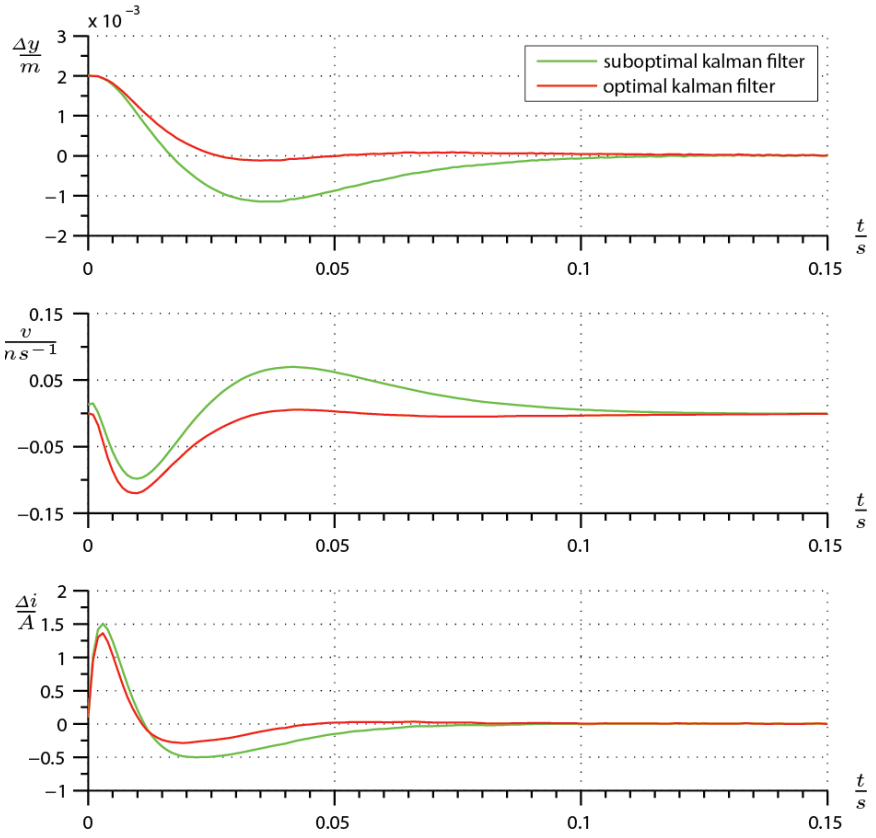

Figure 6.22: Simulation using the estimated velocity in the state feedback

Figure 6.20 shows that the additional calculation effort of the optimal Kalman filter gains control performance at the beginning of the control sequence. After one second, as can be

seen in equation 6.81, the Kalman vector $\underline{K_k}$ can be replaced by $\underline{M}$. Additionally figure 6.22 depicts that the third state $\Delta x_3 = \Delta i$ has been estimated exactly. An application could be the replacement of the sensor signal by the estimated value, if the current sensor is defect. Another possible application could be a plausibility check of the current sensor's signal, to detect deviations.

6.3 State Space Controller in Operation

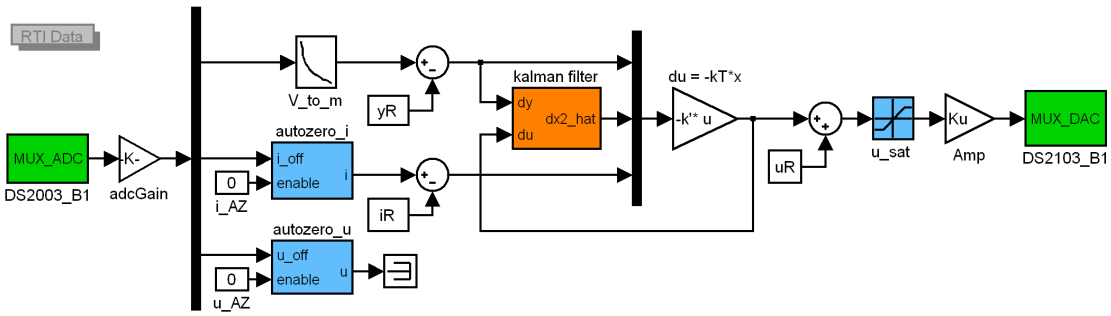

Figure 6.23: Control loop with state feedback using the Kalman filter

The test in figure 6.24 shows the excellent performance of the state space controller with the estimated state Δx_2. The rotor was upheld until $t = -0.2$ seconds and then was suddenly released. The controller stops the falling rotor ideal and holds it in the nominal position $y_R = -5\ mm$.

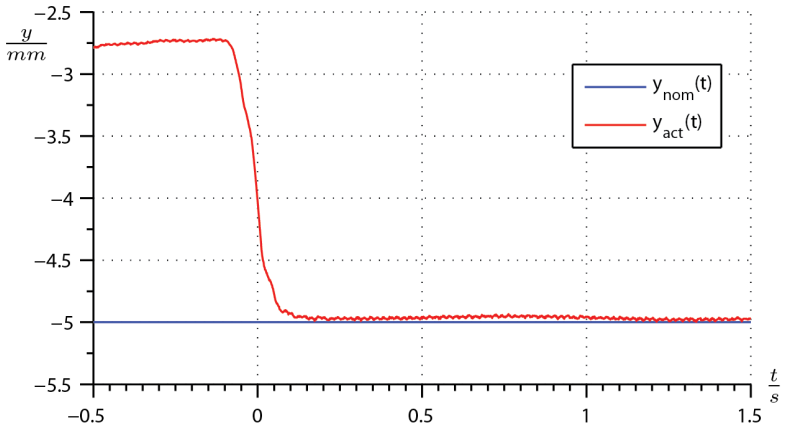

Figure 6.24: Kalman filter test with falling rotor

The test in figure 6.25 is similar to the test in figure 6.24. This time the rotor was held down until $t = -0.1$ seconds and then was suddenly released. The end position is not

exactly $y_R = -5\ mm$ and depends on the exact determination of the state space model's parameters (mass m, inductance ΔL and stand-by current i_R).

Figure 6.24 and figure 6.25 clearly show the advantage of the state space controller. Dynamic processes can be stopped ideally. A disadvantage is that the control error e_∞ is not zero if a perturbation force Δf occurs.

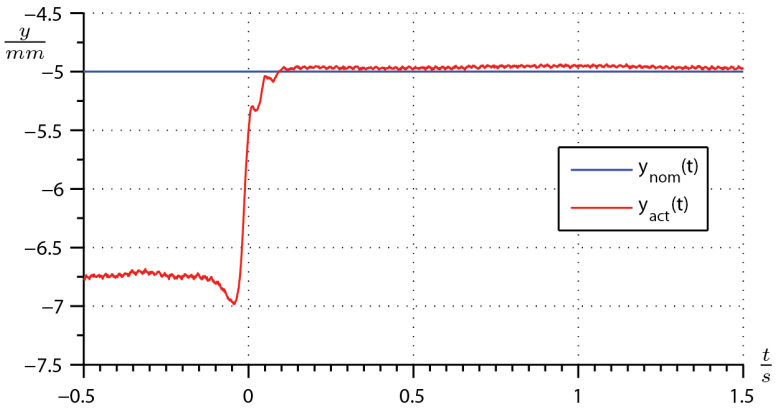

Figure 6.25: Kalman filter test with rising rotor

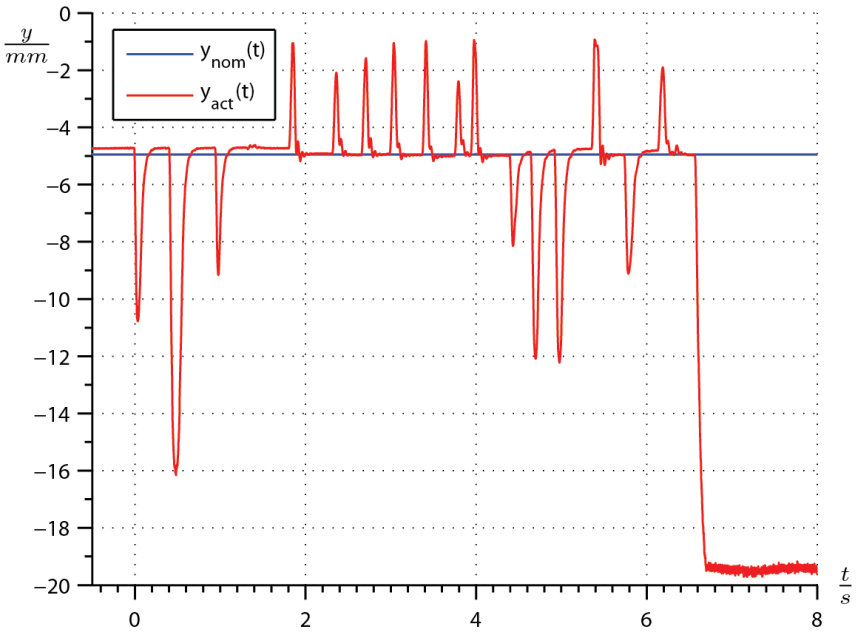

Figure 6.26: Kalman filter test with excessive perturbation

The rotor was pressed downward and upward multiple times. The test in figure 6.26 ended abrupt at $t = 6.8$ seconds. The restoring performance is great when the external

force is gone, nevertheless the rotor's deviations due to external forces should not occur in the first place. To prevent the rotor from deviating, even though an external force Δf occurs, an integrating controller is necessary.

6.4 PID Control Structure

To build up a standard PID[5] controller the first step is to find acceptable parameters for the proportional gain K_p, the integral gain K_i and the differential gain K_d. This is much easier in simulation since the the non-linear electromechanical plant is difficult to control. To start with the simulation the derived plant from section 6.2.1 is used. The PID controller is operated at a sampling frequency of 16 kHz.

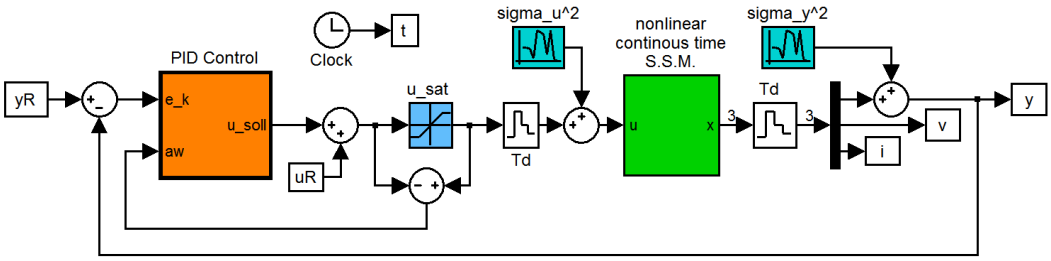

Figure 6.27: Simulink block diagram of the PID control loop

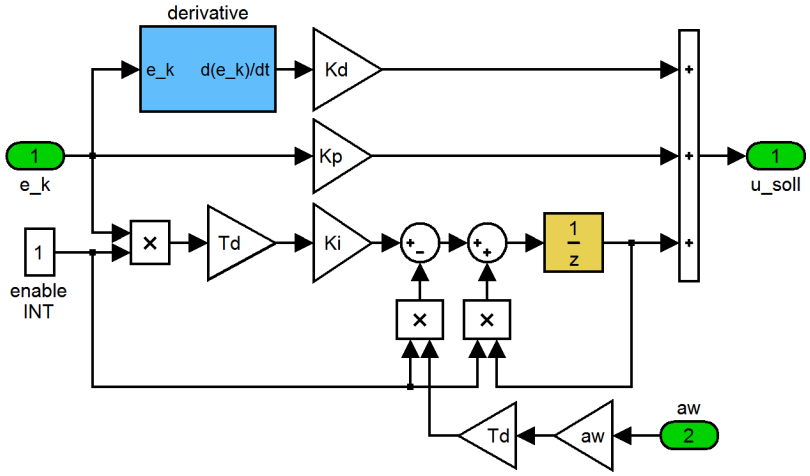

Figure 6.28: Simulink block diagram of the PID controller

The control variable $enable_{INT}$ in figure 6.28 exists to safely deactivate the integrating part. As already mentioned in subsection 6.1.2. It is important to fully deactivate the

[5]Proportional-integral-derivative

integration and anti-windup loop to stop the integration of the control error.

Both, the integrating anti-windup loop and the integrating control loop, need to be scaled with the sampling time T_d to establish independency of the control frequency for the integral gain K_i and the anti-windup gain aw. With this configuration the control frequency of the PID controller can easily be changed at any time. The derivative subsystem in figure 6.28 is of the same type as the derivative $\frac{\partial y}{\partial t}$ with subsequent low pass filtering in figure 6.12 in section "Estimating the rotor's velocity" (section 6.2.5).
Elegant ways to adjust acceptable control parameters are summarized in [11] and this is for instance the tuning method from "Ziegler-Nichols" [6] or the "Autotuning" method [10]. Since those tuning methods did not work in simulation, comparing different PID parameter sets is an optimization task. Therefore the simulation is repeated with a certain step size for one parameter, while the other two parameters are not altered.

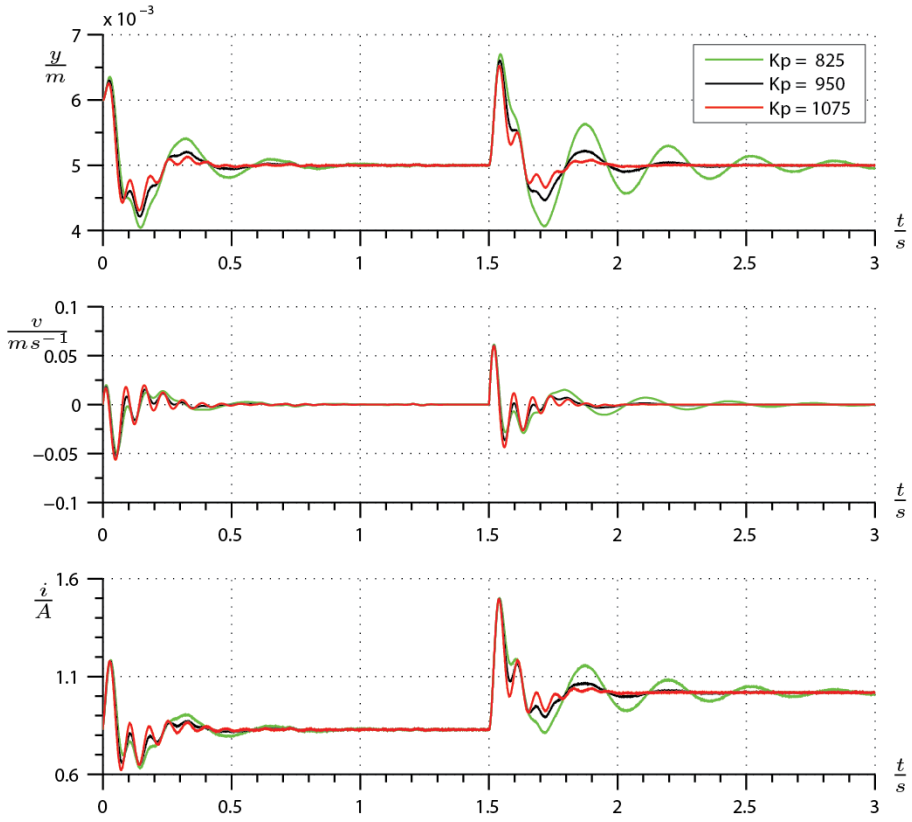

Figure 6.29: Simulation with different values of K_p

For this kind of optimization the simulation starts with a deviated position of 1 mm.

$$\underline{x}_0 = \underline{x}_R = \begin{bmatrix} 0.001 \\ 0 \\ 0 \end{bmatrix} \tag{6.82}$$

At $t = 1.5$ seconds, a perturbation step function $\Delta f = 5$ Newton is added to the value $\ddot{x}_2$ which is the acceleration of y. The simulation proves that the magnetic bearing controlled by a standard controller is capable of handling sudden accelerations. Figure 6.29 shows an improvement in performance by a variation of the proportional gain value K_p.

6.5 PID Controller in Operation

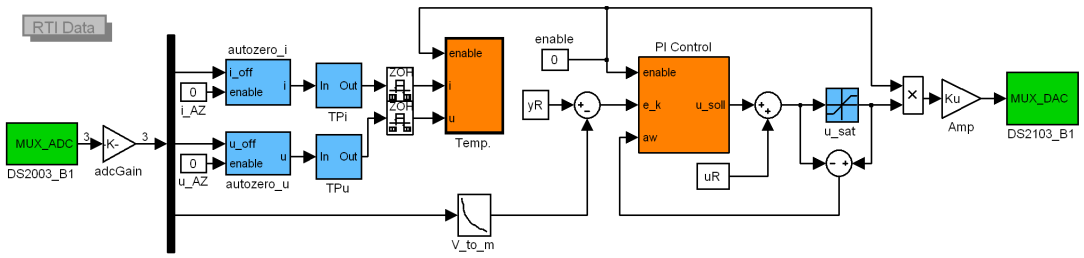

Figure 6.30: PID control loop

Section 6.3 showed that the state space controller is ideal to restore the rotor in its initial position $y_R = -5\ mm$. E.g. the magnetic bearing is powered up. A big disadvantage of the state space controller is that the rotor's position is deviated as long as an external force Δf occurs.

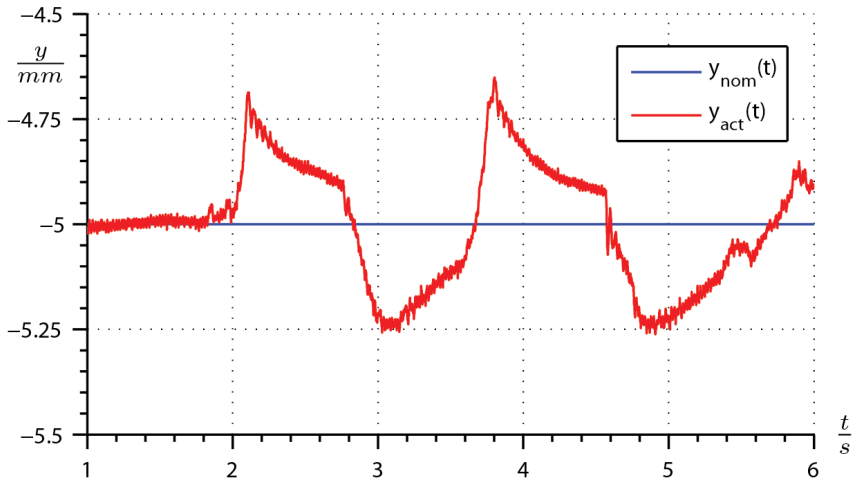

Figure 6.31: PID Controller performance with excessive perturbation Δf

The test in figure 6.31 starts with the rotor in its initial position. What cannot be seen is that the rotor is already loaded with a 0.38 kg-weigh. At $t = 2$ seconds the weight is removed quickly. As a result the rotor moves up and the controller counteracts this movement. At $t = 2.8$ seconds the weight is restored at the rotor again. This proves is repeated at $t = 3.6$ seconds. The test in figure 6.31 shows that an external force of $\Delta f = \pm 3.8\ N$ results in a maximum rotor displacement of $\pm 0.3\ mm$. Therefore an integrating control structure is indispensable for an active magnetic bearing.

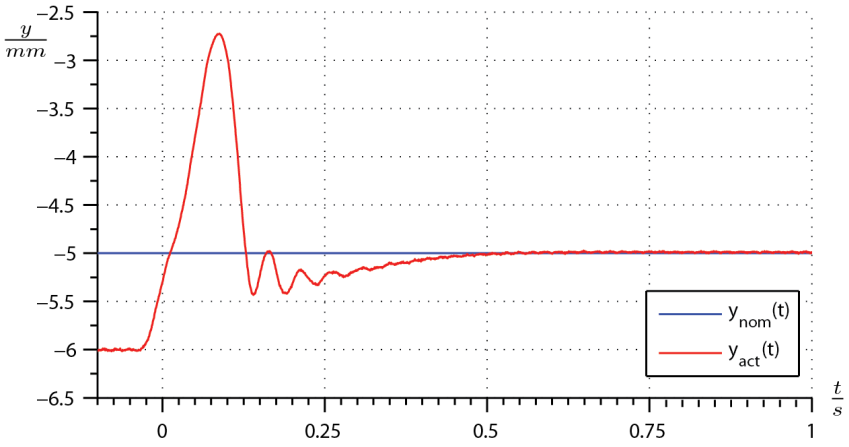

Figure 6.32: PID controller performance

Figure 6.32 shows the performance of the PID controller with the rotor held down until $t = -0.1$ seconds. This test clearly shows the disadvantage of the PID control structure. Dynamic processes are not handled easily because the rotor's velocity v is differentiated from the position signal y. Therefore a combination of the PID control structure with

the state space control structure would be the best configuration.

Chapter 7

Conclusion & Perspective

The primary purpose of this Diploma Thesis was to become acquainted with the active magnetic bearings and its challenges. A subsequent doctoral thesis will intensify my knowledge and experience in this field. In general I realized a simplified active magnetic bearing component that can restore the rotor into it's nominal position y_R when deviated.

A complete active magnetic bearing is obviously more difficult to achieve. For instance the air gap between the electro magnet and the levitated rotor y_R is 5 mm. To enhance the level of efficiency the air gap y_R has to be reduced dramatically. A nominal air gap of $y_R = 1\ mm$ or $y_R = 0.5\ mm$ would be satisfying.

$$100.000\ rpm \rightarrow 1.\dot{6}\ kHz \rightarrow f_c \geq 3.\dot{3}\ kHz \tag{7.1}$$

Control System Since a complete magnetic bearing features contrarily oriented pairs of electro magnets the plant of each bearing component therefore is less non-linear, because a magnetic force f_m can be generated in both directions. To damp possible rotor unbalance the more sophisticated control system needs at least a control frequency that is two or three time higher than twice the rotor's maximum rotational frequency. Equation 7.1 shows that a high speed flywheel operated at a maximum of $n = 100k\ rpm$ requires at least a control frequency f_c of $3.\dot{3}\ kHz$.

Displacement Measurement : The reduced air gap of 0.5 to 1 mm will result in a smaller geometry of the measurement ferrite core. To establish a sampling frequency f_s of $\approx$ 3.3 kHz the ferrite core will be excited with at least 333 kHz. Therefore a sophisticated high frequency iron powder ferrite core will be necessary. Ferrite cores that feature low iron losses up to 500 kHz are available and can be melt in any desired shape. This also requires HF[1] measurement amplifiers and rectifiers that will have to be designed

[1] High frequency

and optimized.

Electromagnet : The sheeted iron core electro magnet is optimal for the basic magnetic bearing component. To enable active rotor damping for a high speed flywheels (HSFWs) the electromagnet should be capable of supplying a 3.3 kHz alternating magnetic field nearly without iron losses. Therefore a sophisticated high magnetic flux iron powder ferrite material will be needed.

Bibliography

[1] Institute of automation and control, university of technology graz - zustandsschätzung und filterung.

[2] Picture from www.ultimatecarpage.com © by dr. ing. h.c. f. porsche.

[3] Rosseta technik gmbh - technical datasheet t1, t2, t3 and t4.

[4] www.porsche.com - porsche 911 gt3 hybrid.

[5] www.spulen.com.

[6] Hägglund T. Aström K. Pid controllers, design and tuning, 2^{nd} edition. Isa, 1994.

[7] Karl Brammer and Gehard Siffling. Kalman-bucy-filter. Ouldenbourg, 1985.

[8] Karl Brammer and Gehard Siffling. Stochastische grundlagen des kalman-bucy-filters. Ouldenbourg, 1986.

[9] E. H. Brandt. Levitation in physics. *Science*, (243):349–355, 1989.

[10] Yu Cheng-Ching. Autotuning of pid controllers. Springer, 1998.

[11] Horn. M Dourdoumas N. Regelungstechnik. Pearson, 2004.

[12] Mårten Sjöström (EPFL-CIRC) Gilbert Schnyder (ABB Secheron S.A.). Hts in power systems. Technical report, 2005.

[13] Helmut Ladler. Entwicklung und realisierung des labormodells "hubmagnet". Master's thesis, University of Technology, Graz, 2002.

[14] Jan Lunze. Regelungstechnik 2. Springer, 1997.

[15] S. L. Ridgway Martin D. Simona, Lee O. Heflinger. Spin stabilized magnetic levitation. Technical report, Department of Physics, University of California at Los Angeles.

[16] Donald A. Bender (Trinity Flywheel Power). Flywheels for renewable energy and power quality applications. Technical report, Energy Storage Association 2000 Annual Meeting.

[17] Peter Radgen. Zukunftsmarkt elektrische energiespeicherung. Technical report, ISI - Karlsruhe.

[18] Prof. Dr. Dirk Uwe Sauer. Optionen zur speicherung elektrischer energie in energieversorgungssystemen mit regenerativer stromerzeugung. Technical report, ISEA - RWTH Aachen.

[19] Gerhard Schweitzer and Eric Maslen. Magnetic bearings. Springer, 2009.

AC	Alternating current
ACF	Auto-correlation function
ADC	Analog to digital converter
AMB	Active magnetic bearing
CAES	Compressed air energy storage
CC	Capital costs
CCD	Charged couples device
CFC	Carbon fiber composite
DC	Direct current
DT1	First order derivative element
DAC	Digital to analog converter
ED	Energy density
EDLC	Electric double layer capacitor, a.k.a. supercap or ultracap
EMAFER	Electro mechanical accumulator for energy re-use
FFT	Fast Fourier transformation
FW	Flywheel

HF	High frequency
HP	High pass
HSFW	High speed flywheel
KFZ	Kraftfahrzeug
LP	Low pass
NaS	Sodium-sulfur battery
NaNiCl	Sodium-nickel-chlorine
PMSM	Permanent magnet synchronous motor
QQ	Quantile-Quantile
PD	Power density
PDF	Power density function
PID	Proportional-integral-derivative
PM	Permanent magnet
PT1	First order lag element
RMS	root mean square
SE	Specific energy
SISO	Single input single output
SMB	Superconducting magnetic bearing
SMES	Superconducting magnetic energy storage
SNR	Signal to noise ratio
SP	Specific power
SRM	Switched reluctance machine
SSM	State Space Model
UPS	Uninteruptible power supply